Influence of key geometrical features on the non-reacting flow of a Lean Direct Injection (LDI) combustor through Large-Eddy Simulation and a Design of Experiments

M. Carreres *, J. García-Tíscar, M. Belmar-Gil, D. Cervelló-Sanz

CMT-Motores Térmicos, Universitat Politècnica de València, Camino de Vera s/n, E-46022, Spain

ABSTRACT

Lean Direct Injection (LDI) emerged as an interesting concept to limit NOx emissions in aero engines at the cost of operating close to the flame lean blow-off limit. In this technology, fuel is injected into a swirled airstream that generates recirculating flow structures that stabilize the flame. It is then of paramount importance at the design stage to understand the effect of various features on these structures. The present investigation makes use of Eulerian-Lagrangian Large-Eddy Simulations (LES) previously validated against existing experimental data for a reference condition to study the liquid non-reacting flow inside the CORIA Spray LDI burner with the help of Adaptive Mesh Refinement (AMR). A Design of Experiments (DoE) is proposed to analyze the significance of several geometrical features on the flow field, namely the combustor width, the air swirler vane angle, the number of swirler vanes and the axial location of the fuel injector tip. The study covers the qualitative appearance of the flow and the quantitative characterization of the spray dispersion and fuel-air mixing process. In this way, the chosen response variables include the size of the relevant coherent flow structures (Central Toroidal Recirculation Zone induced by the Vortex Breakdown Bubble, Corner Recirculation Zone and Swirled Jet) and their associated velocities, spray features (global drop sizes and spray penetration), pressure drop across the swirler and induced swirl number. Besides, the Precessing Vortex Core (PVC) relevance and frequency content is studied through Proper Orthogonal Decomposition (POD). Results from the statistical analysis show that the number of swirler vanes and their angle are the geometrical parameters that most importantly influence the flow features: stronger recirculation zones leading to an improved atomization and mixing have been found both when decreasing the number of swirler blades and increasing the blade angle. However, both solutions also increase the pressure losses across the swirler. As far as the spectral analysis is concerned, the number of swirler vanes is the most influencing factor on both the frequency and intensity of the PVC modes, being crucial for the possible activation and the energetic content of a double-helix PVC mode.

© 2022 The Author(s). Published by Elsevier Masson SAS. This is an open access article under the CC BY-NC-ND license (http://creativecommons.org/licenses/by-nc-nd/4.0/).

1. Introduction

The air traffic growth in the last decades raised concern about the environmental toll of aviation. Institutions such as ICAO (International Civil Aviation Organization) or ACARE (Advisory Council for Aviation Research and Innovation in Europe) envisioned a year 2050 with a 75% reduction in aircraft CO_2 emissions per passenger kilometer, a 90% reduction in terms of NO_x emissions and a noise reduction of a 65% compared to the levels of 2000 [1]. Technological solutions to achieve those stringent goals are needed in areas such as aerodynamics, structures, materials or propulsion systems, among others. Focusing on the latter, Lean Direct Injection (LDI) emerged as a promising NO_x reduction combustion concept [2]. In this technology, fuel is directly injected and surrounded by a swirling airstream responsible for its atomization and its mixing, generally through a recirculating region that acts as an aerodynamic flame holder. While LDI combustors mitigate the risks of auto-ignition and flashback, they operate close to the lean extinction limit. Consequently, several works focus on the blow-off prediction [3–5] and the successive ignition understanding [6–9].

Researchers have performed detailed characterizations of liquid-fueled swirl-stabilized flames with a wide range of experimental techniques in on-purpose test rigs. Some works gave insight into the differences among non-reacting and reacting cases [10,11] or

---

Nomenclature

Abbreviations

ACARE	Advisory Council for Aviation Research and Innovation in Europe
AMR	Adaptive Mesh Refinement
CFD	Computational Fluid Dynamics
CRZ	Central Recirculation Zone
CTRZ	Central Toroidal Recirculation Zone
DMD	Dynamic Mode Decomposition
DOE	Design of Experiments
ICAO	International Civil Aviation Organization
LDI	Lean Direct Injection
LDV	Laser Doppler Velocimetry
LES	Large Eddy Simulation
PDA	Phase Doppler Anemometry
POD	Proper Orthogonal Decomposition
PVC	Precessing Vortex Core
RMS	Root Mean Square
SMD	Sauter Mean Diameter
VBB	Vortex Breakdown Bubble

Greek symbols

α	Heat transfer coefficient
Δt	Time step
Δ	Grid filter
$\delta_{m,l}$	Kronecker delta function referred to the liquid phase
$\dot{\rho}^s$	Exchange function for the source term due to the evaporation of species
ϵ	Turbulent dispersion rate
λ	Thermal conductivity
μ_l	Liquid dynamic viscosity
ϕ	Swirl vane angle
Ψ_i	POD spatial modes
ρ	Density
τ_{PVC}	Precession period of the central vortex
τ_{visc}	Viscous stress tensor
θ	Spray angle
$\widehat{\Delta}$	Test filter

List of notations

$\dot{f}_{bu}$	Droplet breakup source term
$\dot{f}_{coll}$	Droplet collision source term
$\dot{m}$	Mass flow rate
$\dot{Q}_s$	Source term related to spray interactions
$\mathbf{a}_l$	Liquid phase acceleration vector
$\mathbf{u}$	Velocity vector
$\mathbf{x}$	Spatial coordinate vector
B	Mass transfer number
C_μ	Constant for the mass transport diffusion term
C_D	Drag coefficient
c_l	Specific heat of liquid drops
C_{ps}	Empirical constant for the O'Rourke turbulent dispersion model

D	Diffusion term
d_0	Injector exit diameter
d_D	Drop diameter
d_L	Ligament diameter
D_{ext}	External diameter of the swirler exit (reference length)
e	Specific internal energy
F^s	Rate of momentum increase per unit of volume due to the spray
f_{grid}	Grid-scale factor
g	Body forces
h_m	Specific enthalpy of species m
J	Heat flux
k	Turbulent kinetic energy
L_{base}	Base cell size
L_{bu}	Breakup length
L_{ij}	Leonard stress term
L_{scaled}	Scaled cell size
L_v	Specific latent heat for vaporization at constant temperature
M_{ij}	Second filtering operation stress term
N_p	Number of droplets in a parcel
Nu	Nusselt number
Oh	Ohnesorge number
p	Pressure
P_{DN}	Probable number of droplets
Pr	Prandtl number
r	Radial distance
r_0	Drop radius prior to breakup
r_d	Drop radius
R_{ext}	Outer radius of injection
Re	Reynolds number
S_w	Swirl number
S_{ij}	Mean strain rate tensor
S_s	Work done by turbulent eddies to disperse the liquid spray droplets in a parcel
Sc	Schmidt number
Sh	Sherwood number
T	Temperature
t	Time
t_d	Droplet breakup time
U_{ref}	Reference (bulk) velocity at the swirler exit
V_c	Cell volume
V_d	Drop volume
W	Molecular weight
We	Weber number
y	Drop distortion
y^+	Non-dimensional boundary layer distance
Y_v^d	Vapor mass fraction in a cell
Y_F	Fuel mass fraction
Y_v	Vapor mass fraction in a cell
u_θ	Tangential velocity component
u_{rel}	Relative velocity among droplets
u_z	Axial velocity component

the interactions among the gas zones (namely CRZ−Corner Recirculation Zone, CTRZ−Central Toroidal Recirculation Zone, and shear layer) and the liquid droplets thanks to the use of PDA (Phase Doppler Anemometry) or LDV (Laser Doppler Velocimetry) [11,12]. Also, several imaging techniques allowed quantifying the generation of several product species in turbulent spray flames ruled by different co-existing combustion modes and reaction zones. For instance, Masri and Gounder [13] characterized the OH formation in acetone and ethanol flames through LIF (Laser-induced Fluorescence) and Mie-scattering in the Sydney burner. Mulla et al., in turn, used Planar LIF to quantify the OH [14,15], NO$_x$ [14,16] and PAH (polycyclic aromatic hydrocarbons) [15] formation in the CORIA Rouen Spray Burner (CRSB) n-heptane flame, also using LII (Laser-induced Incandescence) to detect soot [15].

The previous efforts have shaped invaluable databases and enabled understanding the combustion of turbulent spray flames in

the quest to reduce pollutant emissions, but their cost hardly allows parametric studies at a design stage. Moreover, the study of turbulent spray flames becomes even more complex with flame-wall interaction in confined burners [17] and the associated thermoacoustic instabilities [18]. Computational Fluid Dynamics (CFD) emerged as a useful tool in this regard. Large-Eddy Simulations (LES) on liquid-fueled combustors have been conducted in both non-reacting [19–21] and reacting test cases with different combustion models [22–28]. Two-phase flow modeling has been performed both through Eulerian-Eulerian (EE) and Eulerian-Lagrangian (EL) approaches. Sanjosé et al. [19] compared these approaches using the same gaseous-phase solver, concluding that both of them are able to capture the opening and rotation of the spray, but attributing more numerical diffusion to the EE formulation in their particular study.

Early studies on swirling flows already noted the strong effect of the swirl vane angle on the existence and size of the central recirculation zone [29], and their combination with convergent or convergent-divergent channels at the swirler exit were also shown to control its size and strength [30]. This led to the so-called swirl-venturi Lean Direct Injection that has been studied with single-point and multi-point configurations [31–33] or to the idea of using variable geometry swirl combustors (VGC) to control the pollutant emissions in different regimes [34].

From here, several studies analyzing the influence of geometrical effects on the combustor flow and performance have been conducted. Focusing on the swirler, Lee and Moon [35] studied the addition of turbulence generators to the swirler vanes, reporting they promote the mixing of fuel and air thus yielding more uniform temperature distributions in the combustor. Tedder et al. [36] analyzed the effect of the swirler vane angle and the injector tip location on the spray angle, Sauter Mean Diameter (SMD) and recirculation zone region, concluding the vane angle has a large effect on the spray angle and the formation of the recirculation zone, characterized by the swirl number S (no recirculation is shaped for $S < 0.6$). They found the injector tip location only shifted the flow without changing its structure, but more uniform droplet distributions were produced the closer the injection tip was to the venturi throat. Sharma et al. [37] reported similar observations on the swirler vane angle and also analyzed the effect of the swirler vane number, finding it less significant than the former. In a gaseous-fueled configuration, Ren et al. [38,39] tried to relate the swirler vane angle to NO_x formation, concluding that a compromise is needed among the vane angle shaping a recirculation zone and increasing the fuel residence time in the combustor. Despite being carried out away from combustors (for a water jet), Oberleithner et al. [40] performed a sweep on the swirl number S, classifying the vortex breakdown (VB) regimes and their intermittency from $S = 1.06$ through PIV (Particle Image Velocimetry) and a FFT (Fast Fourier Transform) and POD (Proper Orthogonal Decomposition) analysis. Thus, they tried to relate the swirl effects not only to the size of the macro structures but also to their frequency content. Other works have focused on the contraction ratio of the airflow right downstream of the fuel atomizer [41], showing that the contraction reduces the corner recirculation zone sensitivity to the outlet geometry, but importantly influencing the central recirculation zone enhancing the strength of the inner vortex core. This work also makes use of DMD (Dynamic Mode Decomposition) to analyze the modes related to the inner vortex core and outer vortex ring.

Besides, some research focused on the combustor geometry. Grinstein and Fureby [42] compared the use of rectangular and circular cross-sections, finding a stronger and more coherent central toroidal vortex in the round combustor which yields a more corrugated flame in the reacting case. Other studies tried to optimize the divergent angle of the combustor inlet wall [43,44], also

noticing its influence on the corner and central recirculation zones and the features of the combustion instabilities, being more largely damped for an intermediate divergent angle [43]. Gejji et al. [45], in turn, studied the effect of the plenum length and combustor length on combustion instabilities through PSD (Power Spectral Density) of the pressure fluctuations, showing the most unstable configuration led to fluctuations as large as 20% of the chamber pressure.

From all the previous studies it is clear that the swirl-venturi arrangement and the burner geometry importantly drive liquid atomization, fuel-air mixing, combustion performance and thermoacoustics. The present investigation introduces a computational study about the significance of several geometrical parameters (namely the combustor width, the air swirler vane angle, the number of swirler vanes and the axial location of the fuel injector tip) on the aforementioned features in a liquid-fueled single-element laboratory confined combustor. The numerical methodology, based on Eulerian-Lagrangian LES conducted with CONVERGE CFD software, has been thoroughly validated against existing experimental data in a previous work for the baseline geometry and the non-reacting condition tested. A Design of Experiments (DoE) is proposed in order to reduce the number of simulations to perform. Several response variables are defined to quantitatively measure the impact on the spray dispersion, on the size and intensity of the flow structures and recirculation regions and on the pressure loss along the swirler, among others. Additionally, the spectral behavior of the self-excited Precessing Vortex Core (PVC) is analyzed in all cases through the application of the POD data-driven technique so as to relate its most important modes to the combustor geometrical features.

2. Numerical methodology

This study used a Eulerian-Lagrangian framework within the CONVERGE CFD software, the Lagrangian side used to model the liquid fuel since in the application of this work the smallest turbulent scales are much bigger than the particles scales. Fuel injection is described by injecting a series of individual parcels containing a certain number of droplets, rather than by a single drop. Each parcel represents a collection of droplets with similar size, location and properties. These droplets are collected from individual parcels before solving the Lagrangian equations for the averaged properties of each parcel, reducing the computational cost of the simulations.

2.1. Governing equations

The mass conservation equation for the multiphase mixture can be described by Eq. (1):

$$\frac{\partial \rho_m}{\partial t} + \nabla \cdot (\rho_m \mathbf{u}) = \nabla \left[\rho D \nabla \cdot \left(\frac{\rho_m}{\rho} \right) \right] + \dot{\rho}^s \delta_{m,l} \tag{1}$$

where ρ_m is the mass density of species m.

The momentum conservation equation for the fluid mixture, including turbulence modeling, is described according to Eq. (2):

$$\frac{\partial \rho \mathbf{u}}{\partial t} + \nabla \cdot (\rho \mathbf{u}\mathbf{u}) = -\nabla p - \nabla \left(\frac{2}{3} \rho \kappa \right) + \nabla \tau_{visc} + F^s + \rho g \tag{2}$$

where τ_{visc} is the total (laminar and turbulent) viscous stress tensor and F^s is the momentum increase rate due to the spray per unit of volume. The viscous stress tensor is related to the diffusion coefficient D and its Newtonian form is given by Eq. (3):

$$\tau_{visc} = \rho D \left[(\nabla \mathbf{u} + \nabla \mathbf{u}^T) - \frac{2}{3} \nabla \cdot \mathbf{u}\mathbf{I} \right] \tag{3}$$

where **I** is a unit dyadic.

The energy conservation equation is described according to Eq. (4):

$$\frac{\partial \rho \epsilon}{\partial t} + \nabla \cdot (\rho \mathbf{u} \epsilon) = -p \nabla \cdot \mathbf{u} - \nabla \cdot J + \rho \varepsilon + \dot{Q}^s \tag{4}$$

Turbulent heat conduction and enthalpy diffusion are accounted for in the heat flux vector J, according to Eq. (5):

$$J = -\lambda \nabla T - \rho D \sum_m h_m \nabla \cdot \left(\frac{\rho_m}{\rho} \right) \tag{5}$$

where h_m is the specific enthalpy of species m. The diffusion term D in Eqs. (1) to (5) is related to the turbulent kinetic energy and its corresponding dissipation rate according to Eq. (6):

$$D = C_\mu \frac{k^2}{\varepsilon} \tag{6}$$

whose terms need to be modeled through a turbulence model.

The so-called spray equation that governs the discrete phase (Eq. (7)) explains the evolution of the droplet distribution through a function f that depicts the probable number of droplets P_{DN} [46]:

$$P_{DN} = f(\mathbf{x}, r_d, \mathbf{u}_l, T_d, y, \dot{y}, t) \, \mathrm{d}\mathbf{x} \, \mathrm{d}r_d \, \mathrm{d}\mathbf{u}_l \, \mathrm{d}T_d \, \mathrm{d}y \, \mathrm{d}\dot{y} \tag{7}$$

The temporal rate of change of the f function can be obtained by solving a Taylor series expansion form of the spray equation, reducing grid effects on the spray:

$$\frac{\partial f}{\partial t} + \nabla_x \cdot (f \mathbf{u}_l) + \nabla_u \cdot (f \alpha_l) + \frac{\partial (f \dot{r}_d)}{\partial r_d} + \frac{\partial (f \dot{T}_d)}{\partial T_d}$$
$$+ \frac{\partial (f \dot{y})}{\partial y} + \frac{\partial (f \ddot{y})}{\partial y} = \dot{f}_{coll} + \dot{f}_{bu} \tag{8}$$

The source terms ($\dot{f}_{coll}$ and $\dot{f}_{bu}$) are originated from droplet collision and breakup, respectively.

The exchange functions $\dot{\rho}^s$, F^s, and $\dot{Q}^s$ for liquid-gas coupling can be obtained by adding up the rate of mass, momentum and energy for all the drops in the spray at position x and time t:

$$\dot{\rho}^s = -\int f \rho_l 4\pi r^2 \dot{r} \, \mathrm{d}\mathbf{u}_l \, \mathrm{d}r_d \, \mathrm{d}T_d \, \mathrm{d}y \, \mathrm{d}\dot{y} \tag{9}$$

$$F^s = -\int f \rho_l \left(\frac{4}{3}\pi r^3 \alpha' + 4\pi r^2 \dot{r} \mathbf{u}_l \right) \mathrm{d}\mathbf{u}_l \, \mathrm{d}r_d \, \mathrm{d}T_d \, \mathrm{d}y \, \mathrm{d}\dot{y} \tag{10}$$

$$\dot{Q}^s = -\int f \rho_l \left\{ 4\pi r^2 \dot{r}_d \left[e_l + \frac{1}{2}(\mathbf{u}_l - \mathbf{u}) \right] \right.$$
$$\left. + \frac{4}{3}\pi r^3 \left[c_l \dot{T}_d + a'(\mathbf{u}_l - \mathbf{u} - \mathbf{u}') \right] \right\} \mathrm{d}\mathbf{u}_l \, \mathrm{d}r_d \, \mathrm{d}T_d \, \mathrm{d}y \, \mathrm{d}\dot{y} \tag{11}$$

where e_l and c_l are the specific internal energy and specific heat of the liquid droplets, respectively. The term $(\mathbf{u}_l - \mathbf{u})$ represents the relative velocity between liquid droplets and gas, while $\mathbf{u}'$ refers to the turbulent velocity fluctuations of the carrier phase.

The velocity of a single drop ($u_{l,i}$) is calculated from its equation of motion:

$$\rho_l V_d \frac{du_{l,i}}{dt} = F_{d,i}$$
$$= C_D \pi r^2 \frac{\rho_g |u_g - u_{l,i}|}{2} (u_g - u_{l,i}) + \rho_l V_d g_i \tag{12}$$

The right-hand side of Eq. (12) is the sum of forces on the droplet $F_{d,i}$, namely aerodynamic and gravitational forces, respectively.

2.2. Relevant submodels

In this section each relevant submodel will be explained briefly. For further details the reader is referred to the original work by the authors containing the validation of the liquid-fueled injection case against existing experimental data [47].

2.2.1. Turbulence modeling

In a previous study, the authors studied the influence of different RANS and LES sub-grid scale models on the gaseous-fueled problem [48], observing the Dynamic Smagorinsky model interacted reasonably with the AMR yielding the best agreement against experimental data. For this reason, this model has been applied in the present work to characterize the unsteady non-reacting flow field.

The generic Smagorinsky model is a zero-equation LES model (i.e., no additional transport equation is solved), which relates the turbulent viscosity to the magnitude of the strain rate tensor and cell size. The model relates the turbulent viscosity to the magnitude of the strain tensor as given by Eq. (13) [49].

$$\tau_{turb,ij} = -2C_S^2 \Delta^2 \bar{S}_{ij} \sqrt{S_{ij} S_{ij}} \tag{13}$$

where, in the Dynamic Smagorinsky model, the Smagorinsky coefficient C_S is dynamically and locally adjusted as per Eq. (14).

$$C_S = \frac{M_{ij} L_{ij}}{M_{kl} L_{kl}} \tag{14}$$

where M_{ij} accounts for a second filtering operation through a test filter $\widehat{\Delta} = 2\Delta$. For more details on the Dynamic Smagorinsky subgrid scale model, the reader may refer to Germano et al. [50].

2.2.2. Atomization and breakup modeling

The TAB (Taylor Analogy Breakup) model by O'Rourke and Amsden [51] has been selected for the liquid injection modeling of the secondary atomization. For more details about the atomization model selection and the equations of the TAB model used in this framework the reader is referred to the previous work by the authors [47].

2.2.3. Drop drag

The drop drag is quantified by the drag coefficient C_D. For thin sprays considering spherical drops, it can be estimated as a function of the drop Reynolds number (Re_d) [52]. For more details on the specific C_D estimation used in this case setup the reader is referred to [47].

2.2.4. Drop turbulent dispersion

In this investigation, a stochastic tracking method has been employed to predict the effect of the turbulent flow on the dispersion of spray drops. This approach adds an instantaneous fluctuating velocity $\mathbf{u}_i'$ to the gas velocity $\mathbf{u}_i$ in the particle trajectory before the integration of Eq. (12). The O'Rourke turbulent dispersion model employed in this study assumes that each component of $\mathbf{u}_i'$ follows a Gaussian distribution. Newton's method is used to numerically obtain the specific values of the cumulative distribution function. The trajectory of each liquid droplet is integrated according to the procedure established by the previous work of the authors [47]. In the end, a drop-eddy interaction time t_d is computed according to Eq. (15) [53] as the minimum of the eddy characteristic lifetime and the time taken by a droplet to travel through the eddy.

$$t_d = min \left[\frac{k}{\epsilon}, C_{ps} \frac{k^{3/2}}{\epsilon} \frac{1}{|\mathbf{u}_i' + \mathbf{u}_i|} - \mathbf{u}_l' \right] \tag{15}$$

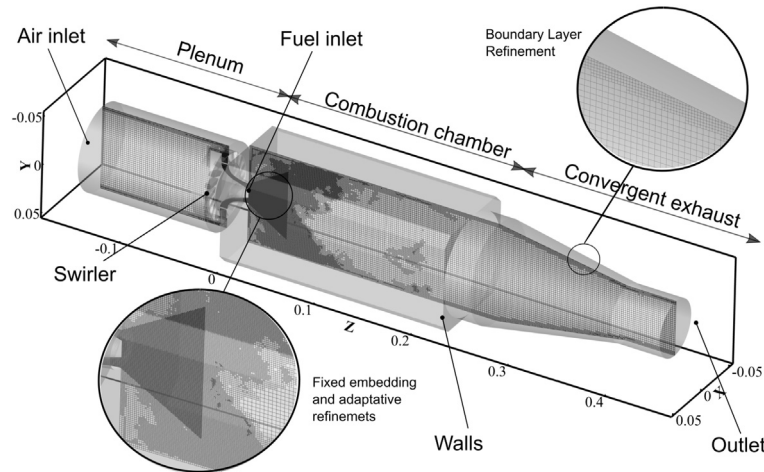where C_{ps} is an empirical constant chosen as 0.03.

Fig. 1. CORIA Spray LDI burner computational domain. The grid of a cross-section illustrates the meshing strategy: 3 levels of fixed embedding in the swirler and injection cone region, AMR and wall refinement.

2.2.5. Drop collision and coalescence

The O'Rourke collision and coalescence model [54] is selected for the study. It implies a stochastic estimation of collisions, assuming that parcels can only collide when they are in the same Eulerian cell. Given that the number of possible droplet collisions scales with the square of the number of droplets, the parcel concept allows estimating the number of droplet collisions in a computationally efficient manner: computing individual droplet collisions for the whole simulation would be unfeasible for this multi-scale problem without the parcel concept. For further details on the model, the reader is referred to the original reference [54].

2.2.6. Drop evaporation

The drop radius rate of change due to vaporization ($\dot{r}$) shown in Eqs. (9) to (11) is calculated with the Frossling correlation [55]. For details on the formulation of the drop evaporation submodel the reader is referred to [47].

2.3. Combustor geometry and boundary conditions

The CORIA Spray LDI experimental burner [56,57], whose 3D sketch is described in Fig. 1, has been employed for validating the CFD code.

The configuration of the burner is composed by four components: a plenum that decelerates the flow before it crosses the swirler, a radial swirler comprised by 18 rectangular channels ($6\,\text{mm} \times 8\,\text{mm}$) sloped 45° (respect to the radial direction) with inner and outer diameters of 10 and 20 mm respectively, a rectangular combustor chamber ($100 \times 100 \times 260\,\text{mm}$) and a convergent duct to avoid flow recirculation.

The flow through the plenum and the swirler vanes is considered in the computational domain, since the flow dynamics and coherent structures are mainly governed by the flow conditions at the swirler outlet.

2.3.1. Boundary conditions

The operating and boundary conditions of this work are homologous to the previous work on the liquid case validation [47], where liquid n-heptane is injected through a simplex pressure swirl atomizer from Danfoss (nominal mass flow rate of 1.46 kg/h, 80° hollow cone) placed in the center of the swirler, at atmospheric pressure ($p = 1$ atm). The simulated condition corresponds to ultra-lean conditions, for which experimental data are available in the literature [56–59]. Its defining parameters are synthesized in Table 1.

Table 1
Operation and boundary conditions simulated.

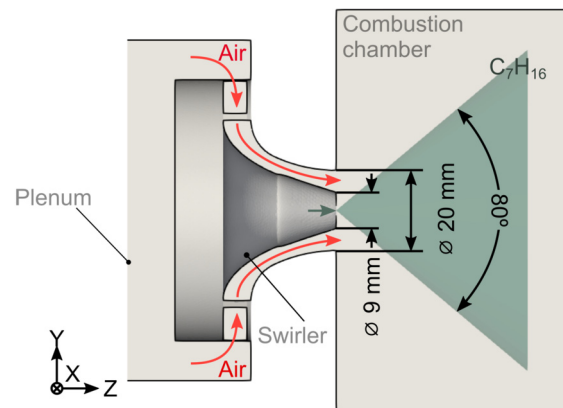| Magnitude	Value
p [atm]	1
T_{air} [K]	416
$T_{C_7H_{16}}$ [K]	350
T_{wall} [K]	387
Plenum injection, $\dot{m}_{air}$ [g/s]	8.2
Central injection, $\dot{m}_{C_7H_{16}}$ [g/s]	0.33
Equivalence ratio [-]	0.61
U_{bulk} [m/s]	70
$\bar{Re}$ [-]	50000

Fig. 2. Swirl-injection system sketch depicting the liquid spray injection strategy.

Air mass flow rate is prescribed at the domain inlet, with a constant pressure imposed at the domain outlet. A no-slip boundary condition is used for all physical walls. Additionally, the O'Rourke and Amsden heat transfer model [54] is used as a law-of-the-wall temperature initial boundary condition to set the temperature at the cell next to the wall by estimating the local fluid-wall heat transfer.

Fuel is injected at the atomizer tip (see Fig. 2), the liquid mass flow rate and temperature imposed according to Table 1. Velocity and drop size experimental data from PDA measurements [56–59] taken at 15-35 mm from the nozzle tip are used to set the spray conditions for the TAB model, which does not consider primary atomization: the Lagrangian parcels are directly injected into the domain according to a Rosin-Rammler distribution with $D_{32} = 31$ µm
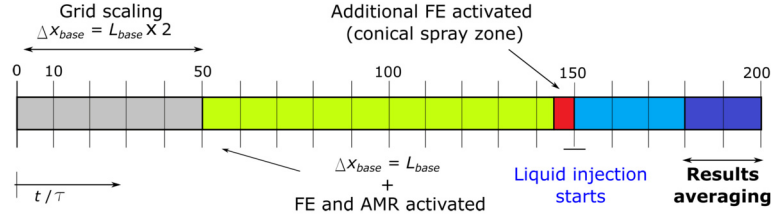
Fig. 3. Sketch of the most relevant events of each simulation.

and a distribution width parameter $q = 2.3$. These values match the experimental data at a location close to the nozzle, but where secondary atomization is already dominant. Additionally, the overall angle of the hollow cone is set to 76° with a thickness of 8°. Nevertheless, the velocity of the injected sheet parcels is determined by the diameter of the nozzle so as to be consistent with the experimental data. The total number of parcels injected was set based on a sensitivity analysis from the literature [60], ensuring that all drop sizes could be represented at least by one parcel. This was achieved dividing the total mass flow rate (0.33 g/s) by the mass of the largest droplet experimentally found (75 μm), yielding 3 million parcels.

2.4. Meshing strategy

The meshing strategy used is analogous to the one employed at the liquid study validation [47]. The 3D domain is discretized in a hexahedral structured grid with a base cell size of 2 mm.

In some areas where better resolution is needed, the cell size is reduced by applying a grid-scale factor f_{grid} as given by Eq. (16):

$$L_{scaled} = \frac{L_{base}}{2^{f_{grid}}} \quad (16)$$

A scale factor $f_{grid} = 3$ is employed as a fixed embedding (i.e., fixed refinement at user-specified locations) to the swirler and a conical near-nozzle region (Fig. 1). In addition, another scale factor $f_{grid} = 2$ has been applied to the adaptive mesh refinement algorithm (AMR) to improve the spatial resolution where the velocity gradient is important (see Fig. 1). In this regard, AMR of y^+ is also used to maintain the correct grid level near the wall ensuring $30 < y^+ < 100$ so that the Werner and Wengle wall model [61] works properly. The total cell count varies at runtime, ranging from 11.5 to 13 million cells in each simulation at all times.

2.5. Numerical algorithms

As in previous works [47,48], a 2nd order discretization scheme is used for the governing equations, while a 2nd order implicit formulation is chosen for time discretization. The Rhie-Chow algorithm [62] is used to prevent spurious oscillations. Meanwhile, the PISO algorithm is used for the pressure-velocity coupling in the transport equations. A variable time-stepping algorithm is used, ensuring that the maximum CFL does not exceed 0.8 in the computational domain. The resulting time steps typically vary from $1.5 \cdot 10^{-6}$ and $2.5 \cdot 10^{-6}$ s, with an average CFL about 0.001.

The liquid-gas momentum coupling approach uses a fully implicit formulation to stabilize the simulation in the presence of small cells and large volume fractions of the liquid. The Taylor series expansion is applied in an iterative algorithm to calculate the drag of all the parcels in each cell and accordingly update the gas phase velocity. Then, this updated gas-phase velocity is used to calculate the drag of all parcels in the cell. This computed force is again used to update the gas-phase velocity until the iterative procedure converges to the specified tolerance.

The adopted timeline of each simulation is shown in Fig. 3, where τ is defined as the time taken for one revolution of the Precessing Vortex Core found in a previous work [47]. In the early stages of the simulation, the mesh is scaled to twice of its base mesh size ($\Delta x = 2 \cdot L_{base}$) in order to stabilize the flow field until the simulation time reaches $t/\tau = 50$. At this moment, the fixed embedding and the AMR start being applied in the swirler region. Each simulation is then run for additional $t/\tau = 100$ to stabilize the velocity field and the overall gaseous mass flow rate. Then, an additional fixed embedding in the conical zone close to the nozzle region is applied $t/\tau = 5$ before the liquid parcels start being injected. Each simulation was then run for additional $t/\tau = 30$ to stabilize the flow and spray field in the final grid strategy before computing temporal averages. Finally, the last $t = 20\tau$ are computed and used to calculate the averaged results analyzed in the investigation.

2.6. Modal decomposition

2.6.1. Proper Orthogonal Decomposition (POD)

POD decomposes the flow into coupled spatial and temporal orthogonal modes sorted by contribution to the flow field energy. The evolution of the flow field in CFD simulations is usually presented in a sequence of N temporal snapshots $\mathbf{v_i}$, gathered in a matrix $\mathbf{V}$:

$$\mathbf{V}_1^N = \mathbf{v}_1, \mathbf{v}_2, ..., \mathbf{v}_N \quad (17)$$

These snapshots need to be separated by a constant time step (Δt_{POD}) and contain M scalar flow magnitudes. One of the main benefits of POD is its ability to reduce the dimension of the arrays, crucial in CFD simulations where output data is arranged in big matrices.

In this work, the $\mathbf{V}$ matrix is decomposed based on the Singular Value Decomposition (SVD) [63], as given by Eq. (18).

$$\mathbf{V} = \mathbf{U} \, \boldsymbol{\Sigma} \, \mathbf{W}^T \quad (18)$$

where $\mathbf{U}$ is a M x N matrix whose columns are the POD spatial modes $\boldsymbol{\Psi_i}$ and constitute an orthonormal basis of V. $\boldsymbol{\Sigma}$, in turn, is a M x N diagonal matrix whose non-zero elements represent the contribution of each spatial mode $\boldsymbol{\Psi_i}$ to the total energy of $\mathbf{V}$. Last, the rows of $\boldsymbol{\Sigma}\mathbf{W^T}$ contain the temporal evolution $\mathbf{a_i}$ of each spatial mode. In short, the overall flow field can be reconstructed as a linear superposition of spatial and temporal data according to Eq. (19).

$$\mathbf{V}(\mathbf{x}, t) = \sum_{i=1}^{N} \boldsymbol{\Psi_i}(\mathbf{x}) \, \mathbf{a_i}(t) \quad (19)$$

For further details about the POD technique formulation used in this study, the reader is referred to a previous work by the authors on modal decomposition techniques in a Lean Premixed injection system [64], i.e. gaseous-fueled.

Table 2
Geometrical parameters and levels considered to conduct the parametric study (values of the baseline geometry highlighted in bold).

Factor	Acronym	Level 1	Level 2	Level 3
Swirler vane angle [°]	A	30	**45**	60
Combustion chamber width [mm]	W	80	**100**	120
Number of swirler vanes [-]	S	6	12	**18**
Axial position of the nozzle tip [mm]	N	**0**	5	10

2.6.2. Data preparation

In order to apply the modal decomposition technique, the cell centroid coordinates and corresponding pressure values are exported to text files (i.e. snapshots). In this study, 200 snapshots are gathered for $t = 20\,\tau$ (recall Fig. 3), implying a spectral resolution of 50 Hz and a sampling frequency of 5 kHz, high enough to apply the Nyquist criterion [65].

POD requires constant spatial coordinates among snapshots, but the AMR algorithm modifies the number of cells at runtime. Hence, the raw data require some preliminary treatment. In a previous step, a subset of 1 million random cells is selected from the first snapshot and taken as spatial reference, providing an adequate compromise between computational cost and spatial resolution. In order to relate the coordinates of the cell centroids of subsequent snapshots, the nearest neighboring cell to each of the reference coordinates is identified. To this end, a *k-d* tree data structure [66] is generated in order to organize the raw coordinates from each new snapshot. A searcher algorithm [67] then computes both the indices of the new snapshot cells that best match the reference coordinates and the Euclidean distance among them. Cells whose computed distance to their corresponding reference is greater than 1 mm are discarded to ensure spatial consistency. Thus, only the pressure values of the accepted cells of a given snapshot are stored in the $\mathbf{v_i}$ vector, finally assembling a consistent **V** matrix.

3. Design of Experiments (DoE) and statistical analysis of variance (ANOVA)

3.0.1. Design of Experiments (DoE)

In complex systems such as LDI burners it is difficult to isolate the separate effect of each of the analysis variables. In such conditions, simple casual associations can be confusing since it is challenging both to establish the causality and to explain specific evidence by looking at individual parts. In this context, Design of Experiments (DoE) techniques may be beneficial to assess the response of the system to the modification of geometrical factors.

In order to understand the interdependencies and trade-offs of various combustor parameters and to optimize the performance of the liquid spray injector, high-fidelity CFD simulations are a crucial tool. In this way the methodology developed and validated against experimental data in previous works [47,48] allows easy changes in design parameters and ensures consistent and comparable accuracy in the outcomes between design iterations.

From the literature [42–45], it is known that the performance of an LDI combustor can be impacted by a significant number of design parameters. In this study, four geometrical parameters with three different levels are considered (see Table 2). However, a full factorial design would lead to 81 (3^4) simulations, so a reduced set from all potential combinations needs to be selected. To this end, a robust design of calculations based on the Taguchi theory [68] is applied to design a systematic set of simulations in which all the level settings appear an equal number of times.

3.0.2. Statistical analysis of variance

The analysis of variance or ANOVA analysis consists of a powerful statistical technique to study the effect of one or more factors among group means. The basic idea is the decomposition of the

Table 3
Taguchi's orthogonal array L9 proposed to study the influence of the geometrical parameters on the non-reacting field (reference case in bold). A: swirler vane angle, W: combustion chamber width (values in the nomenclature are normalized with the external diameter of the swirler exit, $D = 20$ mm), S: number of swirler vanes, N: axial position of the nozzle tip.

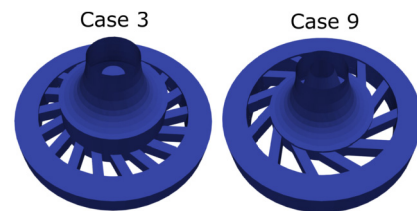| Case	Nomenclature	A [°]	W [mm]	S [-]	N [mm]
1	A30-W4-S6-N0	30	80	6	0
2	A30-W5-S12-N5	30	100	12	5
3	A30-W6-S18-N10	30	120	18	10
4	A45-W4-S12-N10	45	80	12	10
5	**A45-W5-S18-N0**	**45**	**100**	**18**	**0**
6	A45-W6-S6-N5	45	120	6	5
7	A60-W4-S18-N5	60	80	18	5
8	A60-W5-S6-N10	60	100	6	10
9	A60-W6-S12-N0	60	120	12	0

Fig. 4. Detail of the swirler system illustrating the modifications in key features such as the number of swirler vanes, the swirler vane angle and the axial position of the nozzle tip.

total variability observed in some data into the parts associated with each factor considered and a residual part that may include other factors not taken into account. A statistical analysis of variance (ANOVA) of the results from the 9 simulations is performed to identify the individual contribution of the geometrical parameters on the designated response variables. For more details about the ANOVA methodology employed the reader is referred to [69].

3.1. Array selection

The Taguchi method employs a particular set of orthogonal arrays to optimize the number of simulations required to retrieve the full information of all the factors that affect a performance parameter. Following this procedure, a Taguchi's orthogonal array L9 is taken to reduce the study to 9 simulations, compiled in Table 3. The individual contribution of the number of swirler vanes, the swirler vane angle, the combustion chamber width and the axial position of the nozzle tip into both the flow field pattern, the spray size distribution and the occurrence of instabilities in the combustion chamber is evaluated throughout these simulations. Please note that the axial location of the nozzle tip (N) is shifted upstream with respect to the reference case, so level 3 means that the nozzle tip is situated at $z = -10$ mm, as shown in Fig. 4.

3.2. Definition of response variables

The parameters contemplated as response variables in the ANOVA have been selected based on the demand of flow recirculation, jet penetration, air-fuel mixing, proper characterization
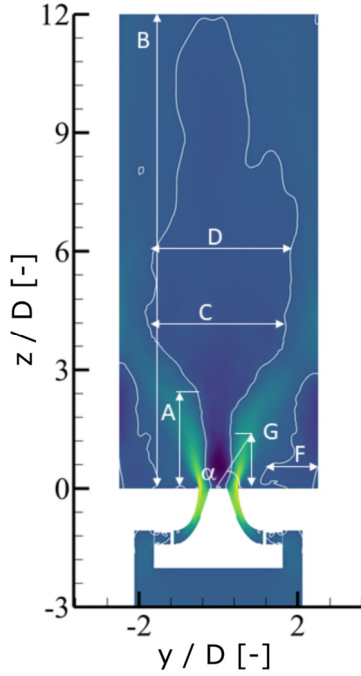
Fig. 5. Definition of some of the response variables considered to characterize the self-excited structures identified through an iso-surface of zero mean streamwise velocity.

Table 4
Definition of the response variables considered for the analysis of variance. The distances and velocities are normalized with the external diameter of the swirler exit and with the mean bulk velocity of the reference case at the swirler exit (D = 20 mm and $\bar{\mathbf{U}}^{ref} = 70$ m/s), respectively. The label of the variables shown in Fig. 5 is also identified.

Label	Acronym	Meaning	Units
A	$L_{VBB,bot}$	Length of the VBB bottleneck	[-]
B	$L_{VBB,top}$	Maximum length of the VBB	[-]
C	W_{VBB}	Maximum width of the VBB	[-]
	U_{CTRZ}^{min}	Minimum axial velocity at the CTRZ	[-]
D	L_{CRZ}	Length of the CRZ	[-]
E	W_{CRZ}	Width of the CRZ	[-]
	S_{CRZ}	Equivalent size of the CRZ ($\sqrt{L_{CRZ} \cdot W_{CRZ}}$)	[-]
	U_{CRZ}^{min}	Minimum axial reverse velocity at the CRZ	[-]
F	$L_{SWJ}^{0.2ref}$	SWJ length with velocity 20% of the baseline	[-]
α	α_{SWJ}	Half SWJ cone angle	[°]
	U_{SWJ}^{max}	Maximum axial velocity at the SWJ	[-]
	V_{SWJ}^{max}	Maximum tangential velocity at the SWJ	[-]
	S_W	Swirl number at the swirler exit plane	[-]
	Δp_{loss}	Pressure loss of the flow along the swirler	[%]
	D_{10}	Global mean arithmetic diameter of the spray	[μm]
	D_{32}	Global Sauter Mean Diameter of the spray	[μm]
	S_{spray}	Spray penetration (axial distance from nozzle tip)	[-]
	f_{PVC}	Frequency of the PVC	[Hz]
	σ_{PVC}	Intensity of the PVC	[-]

of the pressure losses of the flow across the air swirler [70] and to determine the intensity and the frequency of the PVC (see Section 4.3). Some of these parameters are defined from the contour of mean axial velocity depicted in Fig. 5 and further specified in Table 4.

The size and intensity of the large scale coherent flow structures such as the Central Toroidal Recirculation Zone (CTRZ) induced by the Vortex Breakdown Bubble (VBB), the Corner Recirculation Zones (CRZ) and the Swirled Jet (SWJ), are normalized to facilitate comparison between cases. Regarding the spray characterization, both the global drop sizes (D_{10} and D_{32}) and the spray

penetration are considered in the analysis. The latter is defined as the furthest axial distance from the nozzle tip that contains 95% of the liquid fuel mass. Finally, some critical parameters in LDI combustors such as the pressure loss and the swirl number at the swirler exit plane are also computed according to Eqs. (20) and (21):

$$S_w = \frac{1}{R} \frac{\int_0^R \int_0^{2\pi} U V r^2 \, dr \, d\theta}{\int_0^R \int_0^{2\pi} U^2 r \, dr \, d\theta} \qquad (20)$$

$$\Delta p_{loss} = \frac{p_{chamber} - p_{plenum}}{p_{plenum}} \cdot 100 \qquad (21)$$

where U and V represent the axial and tangential velocity components, respectively.

4. Results and discussion

4.1. Influence on the flow variables and self-excited flow structures

A first qualitative representation of the flow pattern is presented through the mean axial and tangential velocity contours of the 9 cases in Fig. 6. Please note that the effects on W_{CRZ} are collected in S_{CRZ} (i.e., $S_{CRZ} = \sqrt{L_{CRZ} \cdot W_{CRZ}}$) as it can be observed in Table 4. The shape, size and intensity of the main structures shift to some extent among simulations, thereby altering the fuel atomization and mixing performance, and affecting the residence time within the combustion region. On the other hand, it is important to highlight that the CTRZ is not originated in Case 3 mainly because the swirl number is below the threshold of the vortex breakdown onset (typically 0.65 in such flows [36]).

The effect of each geometrical factor on the most representative response variables is compiled into the P-value shown in Fig. 7 (the full set of results is provided in Appendix A), where results are represented in the [0, 0.3] range to yield information not only about the most significant parameters on the response variables, but also about other parameters that could be of relevance to a lower extent. At a first glance, it becomes clear that the number of swirler vanes (S) and the angle of these vanes (A) have much more influence on most response variables than the other two geometrical factors. As it may be observed, the former is, by far, the parameter that influences the computed response variables to a greater extent when compared to the effect of the other design parameters. Besides, as it was already observed in Fig. 6, the VBB width is not significantly influenced by any geometric factor.

A closer observation to Fig. 7 allows detecting specific pairs of response variables presenting opposed behavior or tendency. This occurs, for example, between the size/intensity of the CTRZ ($L_{VBB,bot}$, $L_{VBB,top}$ and U_{CTRZ}^{min}) and the size/intensity of the CRZ (L_{CRZ}, S_{CRZ} and U_{CRZ}^{min}), since a larger and stronger CTRZ always leads to smaller and weaker CRZ.

It is important to highlight that, even though the tendency of the response variables related to the maximum and minimum axial velocities could seem opposite to the expected trend, this is only due to the particular way they have been defined. Since the negative sign is conserved in the minimum reverse axial velocities, a negative influence means *more negative* values (i.e., stronger reverse flow). This has to be kept in mind to maintain the consistency in the following reasoning.

Finally, a last recurrent trend between coupled variables can be highlighted: the higher the maximum axial velocity of the swirled jet at the swirler exit region (U_{SWJ}^{max}) the more significant the pressure losses undergone by the flow across the swirler (Δp_{loss}), as expected. This strong correlation requires a trade-off in the combustor design, aiming to achieve adequate mixing and stable flow pattern with minimal pressure loss.
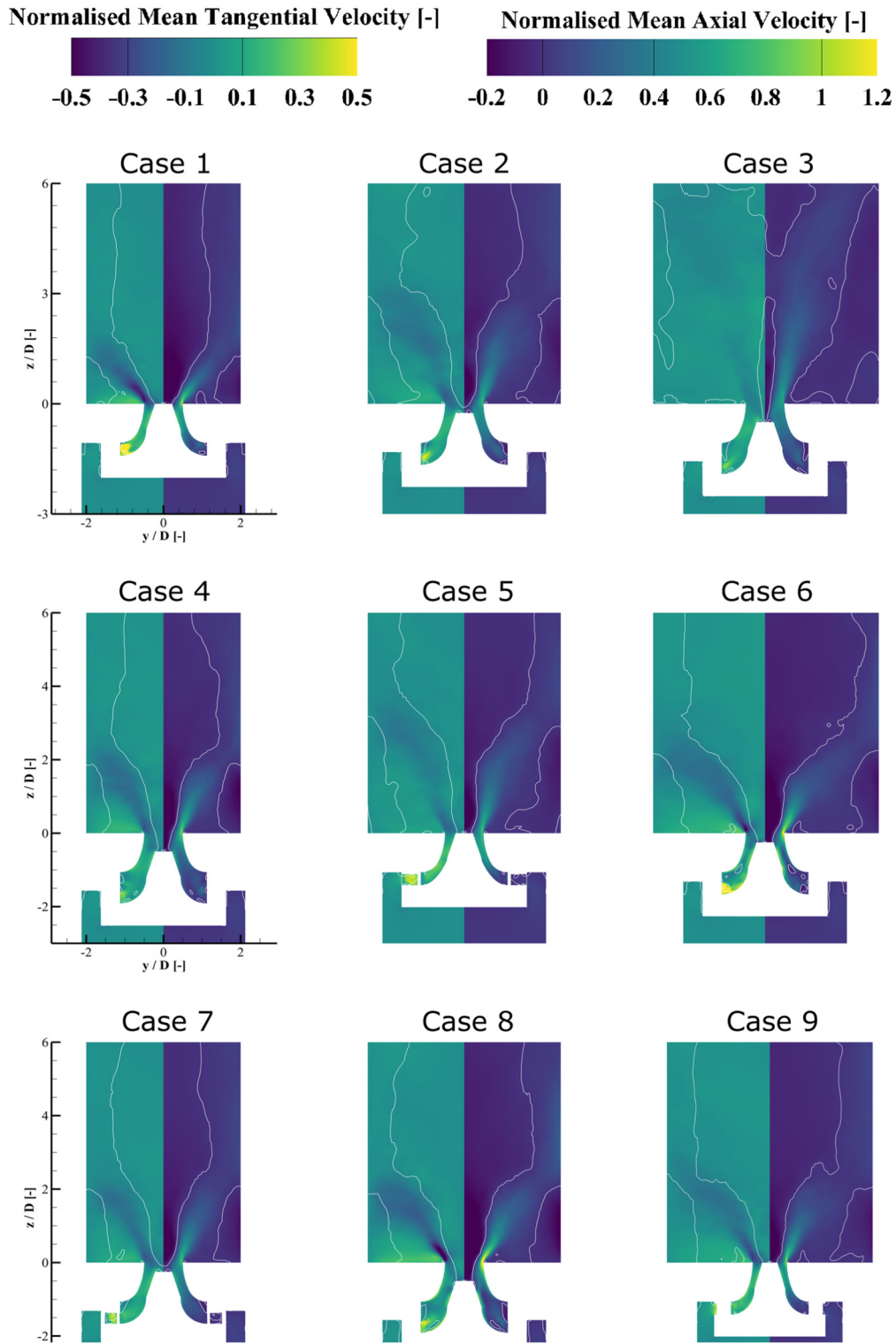
Fig. 6. Contours of time-averaged ($t = 200\tau$) axial (right) and tangential (left) velocity for the simulations of the L9 array. Velocity values are normalized with the mean bulk velocity at the swirler exit of the reference case ($\overline{U}^{ref} = 70\,\text{m/s}$). (For interpretation of the colors in the figures, the reader is referred to the web version of this article.)

Let us now evaluate the influence of each geometrical parameter on the response variables from Fig. 7, starting with the number of vanes of the air swirler (S). It is important to notice that, as the mass flow rate is preserved among simulations, any change in the number of swirler vanes directly leads to a change in the flow velocity obtained across the swirler due to the change of the total effective area. In this way, the higher the number of vanes, the lower the axial (U_{SWJ}^{max}) and tangential (V_{SWJ}^{max}) velocities at

the swirler exit region. Since the tangential velocity component is reduced to a greater extent (in percentage terms) than the axial one, the swirl number (S_W) is considerably decreased (recall that S_W essentially depends on the ratio $U \cdot V / U^2$). Higher numbers of swirl vanes also lead to a substantial decrease of the swirled jet angle (α_{SWJ}), proportionally reducing the intensity of the central recirculating zone (U_{CTRZ}^{min}), ultimately due to the decrease of S_W mentioned above. As a result, an increase in the number of vanes
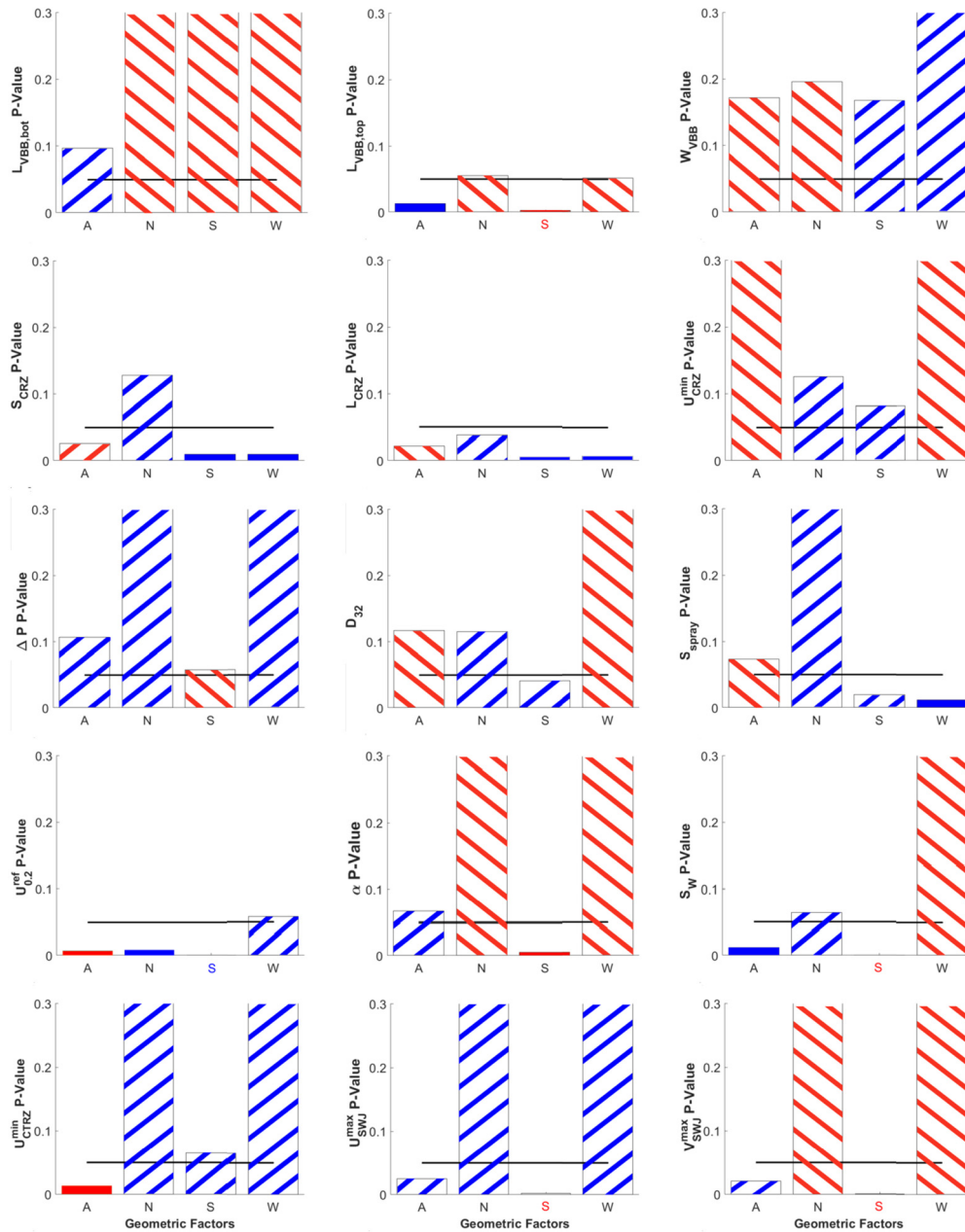
Fig. 7. P-values for the defined response variables and geometrical factors. Blue and red bars represent positive and negative influence on the response variable, respectively. Open bars denote P-value > 0.3 and thick line means P-value = 0.05.

induces a higher spray penetration length and less energetic interactions of the spray with these more turbulent flow structures, which discourages the secondary breakup and assists in reaching higher drop sizes (D_{32}). This conclusion is crucial since the injection model employed is based on a given initial distribution based on a Sauter Mean Diameter. Therefore, the disparity in the final drop sizes reached can be attributed to how the geometry is influencing the atomization phenomenon predicted by the TAB breakup model.

As hinted in Fig. 6, a stronger CTRZ and a faster and more uniform fuel-air mixing are confirmed in the cases presenting a low number of swirl vanes (Cases 6 and 8). Meanwhile, the contrary is appreciated in Cases 3, 5 and 7, as they present higher local fuel concentrations that would lead to subsequent slower-burning rates and unstable aerodynamics flames. This lower spray-air interaction when increasing the number of swirler vanes is also denoted

by the increment of $L_{SWJ}^{0.2ref}$ (see Appendix A), indicating a greater spray penetration, thereby deteriorating fuel distribution.

Nevertheless, an increase in the number of swirl vanes generally results in a significant reduction in pressure losses (ΔP_{loss}). On the other hand, a larger number of swirl blades decreases the length ($L_{VBB,top}$) and width (W_{VBB}) of the VBB, the cases with a smaller number of vanes being those that have a larger CTRZ (Cases 1, 6 and 8 of Fig. 6). Nonetheless, such powerful CTRZ may not be useful or beneficial since it could retain excessively burned products and prevent or difficult their exhaust. Furthermore, it must be considered that an increase of the size and intensity of the CTRZ implies a reduction of the CRZ size (S_{CRZ}) and intensity (U_{CRZ}^{min}) and that an increase in the swirled jet angle means a broader radial spray dispersion. Hence, it could be possible that, with a too low number of swirler vanes, some unburned fuel drops were excluded from entering the primary reaction zone, even not being captured by the (small) CRZ to redirect and feed them to-

wards the combustion zone. Therefore, further research on reacting cases is required for a more consistent evaluation on the role of the CRZs on the specific response variables defined for reacting cases. Only under that circumstance, it will be possible to elucidate if a trade-off between the CTRZ and CRZ is preferred instead of just maximizing the CTRZ.

On the other hand, opposite effects on the response variables to those reported above when increasing the number of swirler vanes (S) are observed (to a lesser extent) when increasing the air swirler angle (A). In this way, the statistical ANOVA confirms that the greater the air swirler angle, the higher the maximum axial and tangential velocity at the swirler exit (the latter again to a greater extent, thus increasing the swirl number), the wider the SWJ angle and the larger and stronger the CTRZ (to the detriment of the CRZ). As mentioned earlier, the characteristics of the CTRZ are deemed to have an important influence on spray penetration length while the higher swirl number results in better atomization.

Consequently, as observed when increasing the number of swirler blades, lower air swirler angle results in larger droplets traveling further downstream along the combustion chamber, thus leading to higher fluctuations of the local equivalence ratio that could promote combustion instabilities in reactive cases. Similarly, the higher the air swirler angles, the higher the pressure losses of the flow across the swirler, although not being as statistically significant as those observed when reducing the number of swirler vanes.

As far as the width of the combustion chamber size (W) is concerned, a low significant influence is generally observed on most response variables. On the one hand, larger corner recirculation zones are generated as the combustor size is increased. This increase leads to a slight reduction in the size/intensity of the CTRZ. Besides, the distance at which the SWJ velocity reaches 20% of the reference is significantly increased, indicating lower and slower diffusion and turbulent mixing at the near-injection zone. Meanwhile, the SWJ angle seems to be slightly reduced when increasing the combustor size, thus involving a moderately greater axial momentum of airflow. Nevertheless, it is difficult to extract conclusions concerning fuel field patterns since this study concerns only non-reacting flow. This precludes the characterization of critical reacting factors such as the lower flammability limit or the flame extent, which are deemed to be crucial requirements to determine the optimal chamber dimensions.

Regarding the axial location of the spray injector tip (N), it is worth recalling that the action of moving the injection system upstream of the swirler exit region also leads to a change in the convergent section found immediately downstream of the swirler vanes entrance (Fig. 4). The more the injection system is shifted upstream, the greater the undiscovered effective section, and therefore the slower the flow velocity achieved across the swirler (similar to the aforementioned effect when increasing the effective area with the number of swirler vanes). In addition, the displacement of the injector also modifies the swirler outlet discharge section to the combustor chamber (at $z/D = 0$), going from a ring of 20 mm and 9 mm of external and internal diameter, respectively, to merely a circular section of $D = 20$ mm. Consequently, it is necessary to separate these possible coupled effects in order to identify the original cause behind the influence on the response variables.

As it can be noticed in Fig. 6, moving the injection system upstream of the swirler exit region produces an increment in the size of the CRZ and therefore a reduction in the VBB and the CTRZ. Since it presents the same tendency as the one observed when increasing the number of swirler blades, the increment in the passage section immediately downstream of the swirler blades entrance can be attributed as the cause. Otherwise, even though the nozzle displacement does not seem to have an evident influence

on the maximum axial and tangential SWJ velocities, a particular impact is observed on the computed swirl number. This slight decrease in the swirl number when moving the spray injection tip upstream is due, therefore, to the change in the swirler discharge section discussed above.

Finally, it could be interesting to introduce some additional images and considerations about the specific influence of the geometrical factors on the response variables. Since the liquid fuel is directly injected in the combustion chamber as a poly-disperse hollow-cone spray, the mixture fraction can undergo inhomogeneities due to fuel stratification that could later lead to undesired unsteady responses of the swirled flame structure. In order to illustrate the variation in spray parcels behavior and mixing performance with the changes in geometry, a qualitative comparison concerning spray dispersion and the equivalence ratio field is shown in Fig. 8. This description reveals a transition in the liquid distribution among cases in line with the transition in flow states reported in Fig. 6. As it can be seen in Fig. 8, the spray pattern is sensitive to the swirl intensity and, thereby, the number of droplets detected in the center of the hollow cone rises with increasing air swirler angle and decreasing number of swirler vanes. On the other hand, in the opposite extreme case (i.e., Case 3, with 18 vanes at 30°), the recirculating flow patterns are not even generated, and the liquid spray cone trajectory travels practically undisturbed, thereby preventing proper atomization and dispersion with incoming swirled air.

4.2. Note about the non-linearities on the response variables

A brief discussion about the non-linearity results is here presented in order to better define the scope of the ANOVA analysis. The ANOVA analysis has been valuable to identify and quantify the global influence of the geometrical factors on the response variables, but at the risk of precluding/masking specific trends of the outcomes with the geometry levels.

Therefore, some selected examples on the dispersion results of several response variables are presented in Fig. 9 (full set of results in Appendix A) in an attempt to overcome the aforementioned limitations related to the linear assumptions and to shed some light for a better interpretation of the non-linear behavior. The reader is referred to the Appendix for the complete set of dispersion results concerning both the whole response variables and design factors. These dispersion graphs allow important observations on how a given response variable changes when the values of each factor are modified.

On the one hand, the dispersion results reinforce some of the reasoning of the ANOVA analysis. For example, as it may be appreciated in the first row of plots in Fig. 9, the maximum tangential velocity at the swirler outlet region (V_{SWJ}^{max}) varies less than axial one (U_{SWJ}^{max}) when the number of swirler vanes (S) is increased, thus resulting in the aforementioned considerable variation in the swirl number (S_W). Besides, the strong correlation highlighted from the P-values between both U_{SWJ}^{max}, V_{SWJ}^{max} and U_{CRTZ}^{min} (please recall the sign convention for reverse axial velocities) can be here better appreciated.

On the other hand, the dispersion scatterplot can also be helpful to clarify and expand the conclusions obtained from the statistical analysis. As discussed, the greater the number of swirler blades (S) reduces the length ($L_{VBB,top}$) of the VBB, but the P-value results attributed a not statistically significance (with a 95% of confidence, i.e., P-value > 0.05) to the width of the VBB (W_{VBB}) and the length of the bottle-neck ($L_{VBB,bot}$). Nonetheless, as it can be seen in the second row of images in Fig. 9, even though the low influence of the number of swirler vanes on W_{VBB} is reinforced, the low influence trend on $L_{VBB,bot}$ is more inconclusive since the
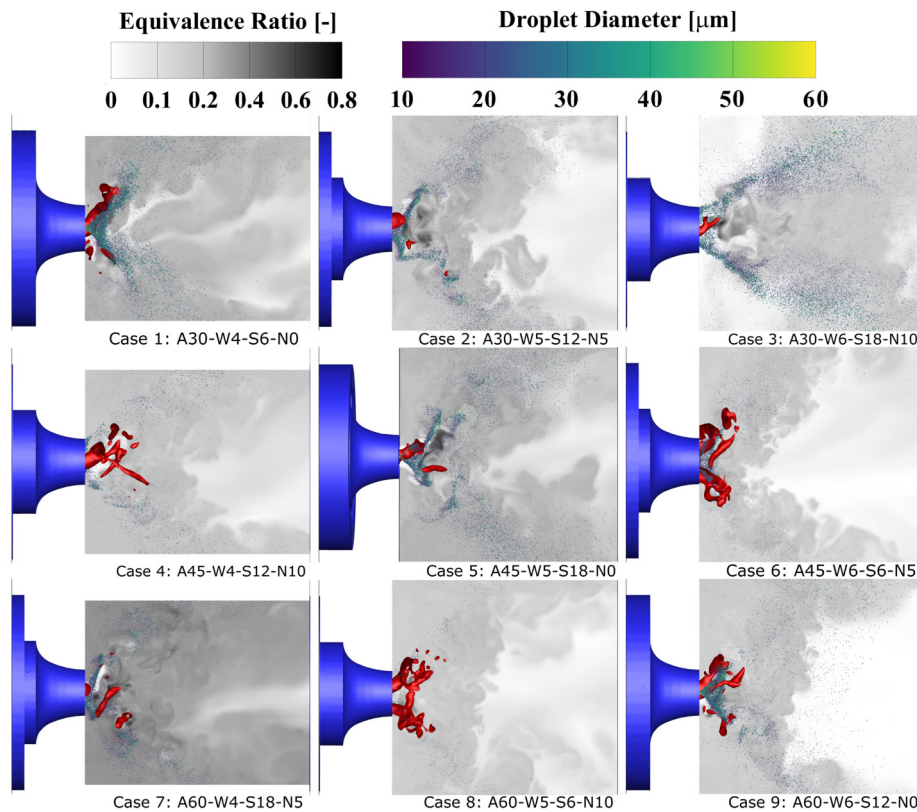
Fig. 8. Representation of the spray pattern (instantaneous parcels), fuel reaction rate (dark-colored) and PVC defined as an iso-surface of pressure (red) at $t = 200\tau$ for the simulations of the L9 array.

high spread induced by the exceptional value of Case 3 appears to be masking the trend showing misleading P-values.

A similar conclusion can be extracted from the dispersion pattern of the W_{VBB} with respect to the width of the combustion chamber (W). A distorted result was displayed in the ANOVA results (P-value of 0.64) because of the low value presented in Case 3. Nevertheless, Fig. 9 manifests an apparent growing trend with the combustor width but moderately by the value of Case 3. This makes it evident that detailed observation of these complementary results (see Appendix) is prudent and necessary to reveal key design parameters not detected as statistically significant at a first glance but that could be relevant on the response variables.

Similarly, the influence highlighted and discussed in the ANOVA analysis about pressure losses with the number and angle of the swirler vanes is here confirmed: the higher the swirler vanes angle (A), the higher the pressure losses across the swirler (ΔP_{loss}), although not being determined as statistically significant by the ANOVA (i.e., P-Value = 0.107) as those observed when reducing the number of swirl vanes (S). Besides, the higher the number of vanes, the lower the non-linearity and the less critical the variation between levels, to the point where little reductions in pressure losses are reported for the cases concerning 18 swirler blades with respect to its homologous of 12 vanes. This fact, together with the significantly worse degree of atomization and spray penetration when increasing the number of vanes, gives an initial conception of a potential path towards a trade-off optimization between pressure losses and atomization performance.

Furthermore, the dispersion results can be useful to reinforce the conclusions about the possible coupled effects originated when shifting the axial location of the spray injector tip (N) in order to identify and associate the original cause behind the influence on the response variables. In this way, the observation of (for example) the patterns concerning the maximum axial velocity at the

swirler outlet (U_{SWJ}^{max}) can be compared between the number of swirler vanes (S) and axial position of the nozzle (N) to elucidate and better attribute the specific causality (e.g., the 3 points corresponding to those cases with 6 swirler vanes are explicitly revealed).

Please note that this study can work as a starting point of a Multi Response Optimization (MRO) in which an analysis can be performed to obtain a trade-off design to maximize/minimize the desired response variables. A Figure of Merit (FoM) or a Cost Function (CF) could be derived from the analysis here presented in an effort to quantitatively characterize the performance of the LDI combustor towards an optimal design trade-off. Nevertheless, these quantities would need to consider additional contributions related to specific response variables defined for reacting cases, such as combustion efficiencies and/or even NOx emissions levels, since they would definitely influence the weighing factors that could be defined from the present study concerning non-reacting flow.

4.3. Influence on the PVC spectral features

A spectral analysis is finally conducted to the L9 array in order to complete the previous discussion through a quantitative characterization of the governing large-scale coherent structure within the LDI burner: the Precessing Vortex Core (PVC). An in-depth definition of the PVC is crucial since its self-excited generation can provoke thermoacoustic oscillations and modulate the fuel distribution, thus altering the combustion process (e.g., the location of the flame front). Besides, the characterization of the PVC in non-reacting cases is justified since it has been demonstrated to reappear after being suppressed at low equivalence ratios due to the coupling of swirled flames with acoustic modes [71].

In this way, following the procedure shown in Section 2.6, the energy contribution and spatial distribution of each POD mode
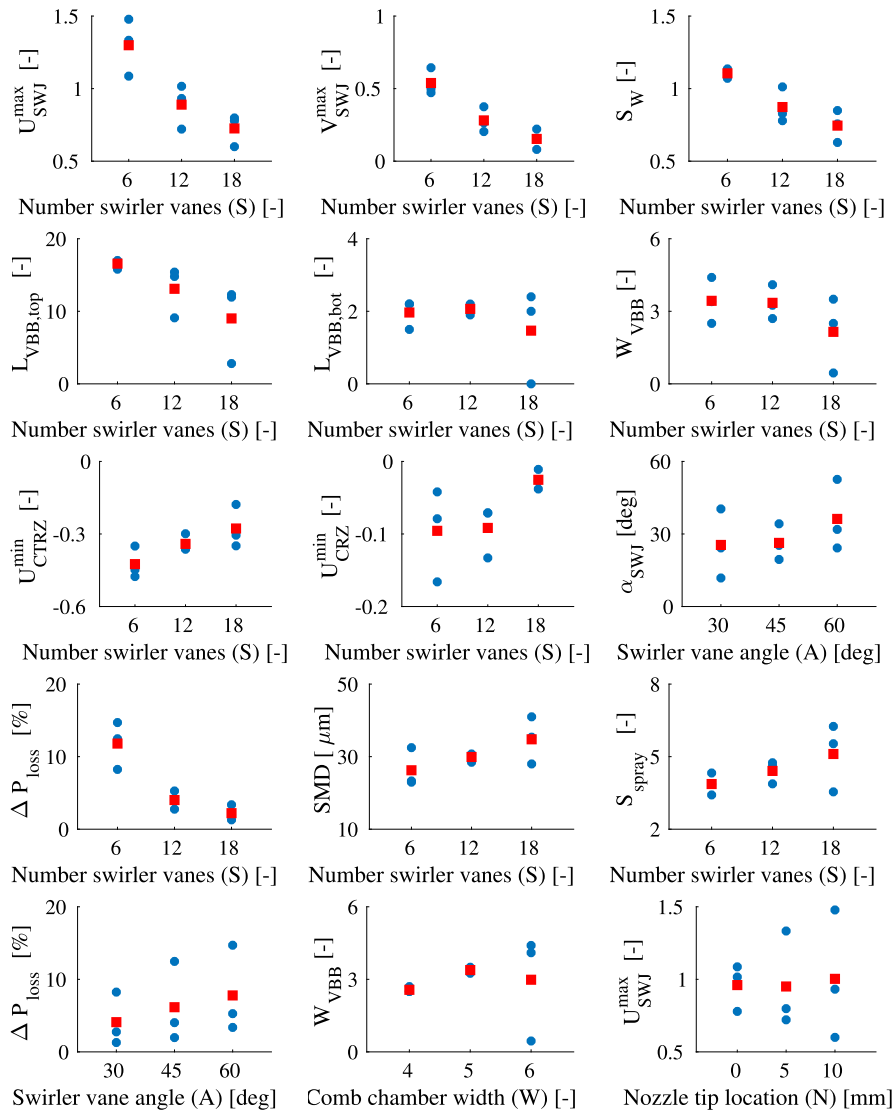
Fig. 9. Dispersion values of sample response variables as a function of a given design parameter. Blue circles: the values of the response variable for each of the 9 simulations. Red squares: average of the 3 values for each level of the considered geometrical factor.

have been obtained from the instantaneous 3D pressure field for each simulation of the L9 array (see Fig. 10). Besides, both the frequency and intensity/amplitude of the detected modes have been compiled in Table 5 for a quantitative comparison between cases. Recall that the singular values σ_i represent the contribution of each orthonormal spatial mode Ψ_i to the total energy of the $\mathbf{V}$ matrix. For this reason, they have been selected as a response variable to quantify the relevance of each POD mode on the total flow field.

As it can be observed in Fig. 10 and Table 5, the changes in key design parameters produce a substantial impact on the energy spectrum due to the way the hydrodynamic modes interact and couple with the acoustic ones. Generally, the dominant PVC mode corresponding to the single-helical PVC structure (1st harmonic) is in the 1.1 - 2.2 kHz range, whereas a 2.1 - 3.6 kHz range is detected in those cases where the double helix PVC (2nd harmonic) is manifested. It is important to note how the energy content in Cases 6 and 8 is much more intense than in all other cases. This result can be explained by the higher pressure losses experienced by those cases, which could finally lead to higher pressure oscillations and thus, higher instability amplitudes. Therefore, this pressure loss along the swirler, together with the one exerted by

the high velocity at the swirler outlet, seems to be critical to the PVC dynamics.

Furthermore, the high σ_i values exhibited by the cases with a lower number of swirler vanes (Cases 1, 6 and 8) are associated to the double-helical PVC structure. In fact, these powerful double-helix modes are also observed to present higher frequencies than those manifested by the cases with a higher number of swirler vanes (i.e., Cases 3, 5 and 7 with both lower frequencies and an insignificant double-helical PVC).

On the other hand, a particular behavior is observed in Cases 1 and 4, which present a similar energy content referred to both pairs of modes (see Table 5), thus indicating the PVC is undergoing a higher and faster alternation between 1 and 2 branches. This could be detrimental since it could provoke stronger thermoacoustic oscillations than the ones produced by a more stable (although powerful) single or doubled-branched PVC.

Analogously to what was done in Section 4, the effects of each geometrical factor on both the frequency and intensity of the two main PVC modes are compiled into the P-value in Fig. 11, whereas their dispersion values are shown in Fig. 12. Several conclusions can be extracted from here:
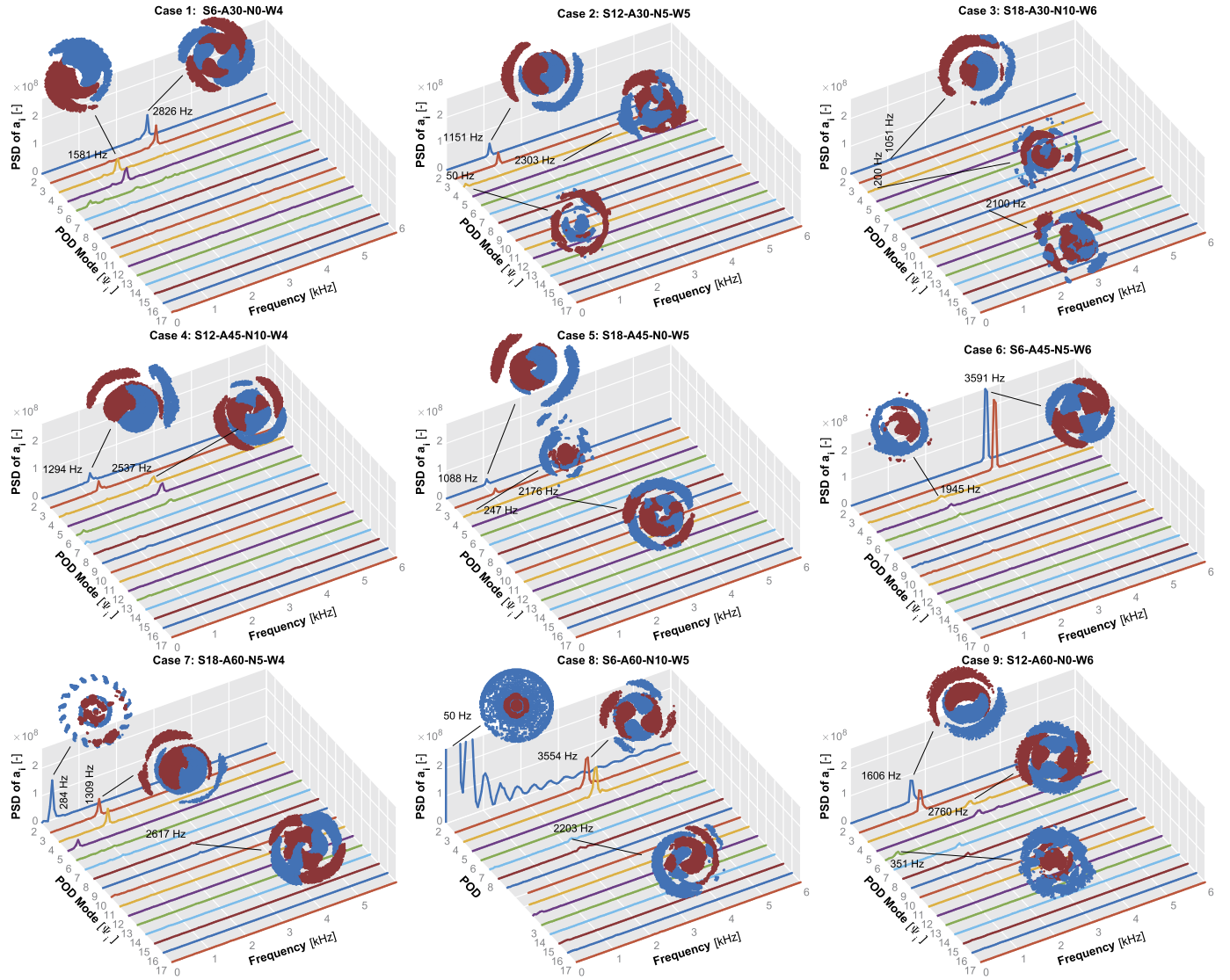
Fig. 10. Power Spectral Density (PSD) and spatial distribution of the time coefficient associated with POD modes $\Psi_2 - \Psi_{17}$ obtained from the 3D pressure signal for each simulation of the L9 array.

Table 5
Frequency and intensity associated to the POD modes obtained from the 3D pressure signal for each simulation of the L9 array. Values in bold denote the most energetic POD mode.

Case	PVC mode					
	1st harmonic			2nd harmonic		
	Modes	Frequency	σ_i [-]	Modes	Frequency	σ_i [-]
1	Ψ_4-Ψ_5	1581 Hz	$2.28 \cdot 10^6$	Ψ_2-Ψ_3	**2826 Hz**	$2.55 \cdot 10^6$
2	Ψ_2-Ψ_3	**1151 Hz**	$1.71 \cdot 10^6$	Ψ_5-Ψ_6	2303 Hz	$0.58 \cdot 10^6$
3	Ψ_2-Ψ_3	**1051 Hz**	$0.56 \cdot 10^6$	Ψ_9-Ψ_{10}	2100 Hz	$0.28 \cdot 10^6$
4	Ψ_2-Ψ_3	**1294 Hz**	$2.05 \cdot 10^6$	Ψ_4-Ψ_5	2537 Hz	$1.85 \cdot 10^6$
5	Ψ_2-Ψ_3	**1088 Hz**	$1.10 \cdot 10^6$	Ψ_5-Ψ_6	2176 Hz	$0.65 \cdot 10^6$
6	Ψ_5-Ψ_6	1945 Hz	$1.40 \cdot 10^6$	Ψ_2-Ψ_3	**3591 Hz**	$4.80 \cdot 10^6$
7	Ψ_3-Ψ_4	**1309 Hz**	$2.05 \cdot 10^6$	Ψ_8-Ψ_9	2617 Hz	$0.81 \cdot 10^6$
8	Ψ_7-Ψ_8	2203 Hz	$1.41 \cdot 10^6$	Ψ_3-Ψ_4	**3554 Hz**	$2.93 \cdot 10^6$
9	Ψ_2-Ψ_3	**1606 Hz**	$2.77 \cdot 10^6$	Ψ_4-Ψ_5	2760 Hz	$1.73 \cdot 10^6$

- The number of swirler vanes (S) stands as the most influencing factor on both the frequency and intensity of the PVC. In this way, the higher the number of blades, the smaller the rotating velocity and the associated energy of the PVC. Besides, the strong influence of S on the presence of an energetic

- double-helix PVC is here confirmed, being the exclusive geometrical parameter with remarkable statistical influence on its intensity ($\sigma_{PVC,2}$).

- A joint look at Fig. 12 and Fig. 7 reveals a strong correlation among the responses of $\sigma_{PVC,2}$ and ΔP_{loss} to the change of S.
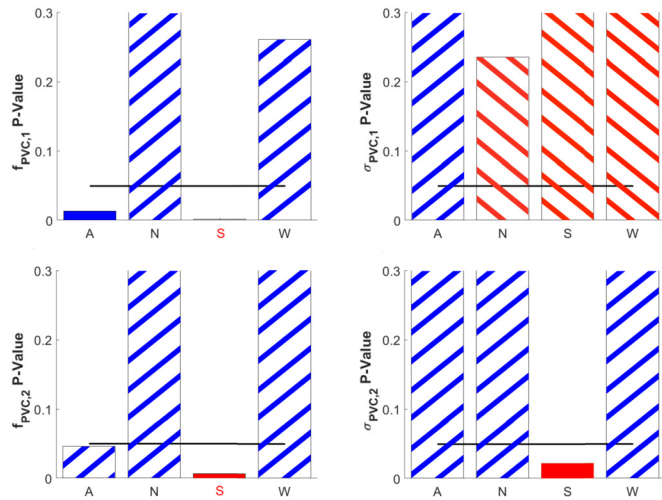
Fig. 11. P-values for the response variables of the POD study. Blue and red bars represent positive and negative influences on the response variable, respectively. Open bars denote P-value > 0.3 and thick line means P-value = 0.05.

This observation reinforces the previous reasoning about the possible dependence of the two-branch PVC intensity and the pressure losses.

- The frequency of both the single and double-helical PVC is strongly affected by the angle of the swirler vanes (A), as expected from the rotation time scale associated to the PVC. This is justified due to the interdependence between the swirler vane angle and the tangential velocity component at the swirler outlet region, as demonstrated in Fig. 7.
- No significant influence of the location of the nozzle tip (N) and the combustion chamber width (W) is noticed on the PVC frequency and intensity. In some literature studies concerning reacting cases [45], it is hypothesized that a shift of the injector tip position may lead to nonlinear distortions on the flame, thus affecting the acoustic oscillations and consequently the instability amplitudes and dominant pressure modes. Nevertheless, the axial placement of the spray injector is not essential for the characteristics of the detected modes in the non-reacting flow and the LDI geometry here investigated.
- The intensity of the single-helical PVC is not affected in a statistically significant manner by any geometrical factor (dispersion graphs shown in Fig. 12). Nevertheless, it seems to be closely related and follow the same trends that the size of the vortex breakdown bubble ($L_{VBB,bot}$ and $L_{VBB,top}$) and the maximum tangential velocity component (V_{SWJ}^{max}). Besides, the intensity of the single-branch presents the opposite trend of the spray penetration (S_{spray}) and the swirled-air diffusion length ($L_{SWJ}^{0.2ref}$) by inducing a shorter fuel penetration length and enhancing the fuel-air mixing.

5. Conclusions

On the basis of a computational model previously validated by the authors, this research has been undertaken to elucidate the effects of key geometrical parameters on the non-reacting flow field and air-fuel mixing characteristics within an LDI burner. A Design of Experiments (DoE) has been proposed to quantify the influence of critical design factors on the defined response variables. In this way, the individual contribution of some functional parameters (namely the number of swirler vanes, the swirler vane angle, the combustion chamber width and the axial position of the nozzle tip) into both the flow field pattern, the spray size distribution and the occurrence of instabilities in the combustion chamber are evaluated through a Taguchi's orthogonal array L9. This technique

allowed minimizing the number of simulations required to provide information on all the factors that affect a specific performance parameter.

From the statistical study, it has become clear that most response variable outcomes mainly depend on the factors linked to the swirler (i.e., the number and angle of the swirler vanes). In this regard, stronger recirculation zones leading to an improved atomization and mixing performance have been found both when decreasing the number of swirler blades and increasing the vane angle. Nevertheless, it has also been noticed how the higher the global degree of atomization achieved, the more significant the pressure losses undergone by the flow across the swirler (this influence is more important for a low number of swirler vanes). Therefore, this strong correlation requires a trade-off in the combustor design, aiming to achieve adequate mixing and a stable flow pattern with minimal pressure loss.

As far as the width of the combustion chamber size is concerned, a low significant influence is generally observed on most response variables. The lower the combustion chamber width, the more concentrated the fuel is in the available volume and the smaller the corner recirculation zones. Nevertheless, it is difficult to extract conclusions concerning fuel field patterns since this study concerns only non-reacting flow. Therefore, it precludes the characterization of critical reacting factors such as the lower flammability limit or the flame extent, which are deemed to be crucial requirements to determine the optimal chamber dimensions.

On the other hand, it can be demonstrated that shifting the location of the nozzle tip upstream can have a beneficial effect on the resulting spray atomization, despite not being significant from the statistical point of view. This can be justified by the larger distances (higher residence time) that the liquid sheet will have to interact with the flow structures. Since the flow structures are not quite influenced by the nozzle tip location, it could seem beneficial to move it upstream as much as possible. Nevertheless, a trade-off could appear at real-engine operating conditions since displacing it too much upstream would imply abandoning the direct injection strategy itself, tending to partially premixed combustion. This could promote the appearance of flashback with the consequent damage to the swirler structure.

The ANOVA analysis has been valuable to identify and quantify the specific global influence of the geometrical factors on the response variables, but at the risk of precluding/masking specific trends of the outcomes with the geometry levels. For this reason, a brief discussion about the non-linearity on the dispersion results has allowed a better definition of both the scope and limitations (related to linear assumptions) of the statistical analysis.

Finally, the governing Precessing Vortex Core has been quantitatively characterized through the POD technique. In this way, the spectral analysis has revealed how a geometrical modification can redistribute the energy between detected modes, changing their frequency, intensity and shape, and thus activating particular modes that can become more important than in the baseline case. The number of swirler vanes has been again observed to be the most influencing factor on both the frequency and intensity of the PVC. In this regard, the higher the number of swirler blades, the smaller the rotating velocity and the associated energy of the PVC. Besides, the number of swirler blades has been revealed to be crucial into both the activation and the energetic content of the double-helix PVC.

In conclusion, such a statistical study constitutes a good starting point for subsequent studies of injection, atomization and combustion on LDI burners. The methodology here presented can be exploited as a potential tool in the design phase, allowing to optimize the performance of the LDI combustor towards an optimal design trade-off at a faster and lower cost than the one that an
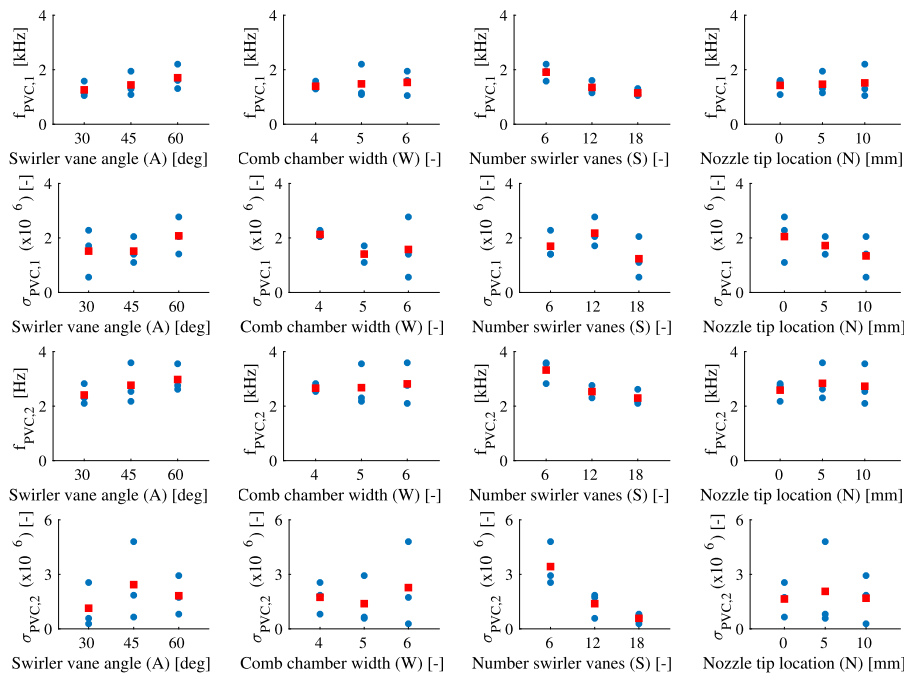
Fig. 12. Dispersion values of the spectral response variables for each design parameter. Blue circles: the values of the response variable for each of the 9 simulations. Red squares: average of the 3 values for each level of the considered geometric factor.

experimental campaign would imply. Nevertheless, the selection of the definite response variables to optimize and the high sensitivity of the calculated optimal solution to the user-defined weights applied to each response variable precludes any concluding optimization from a non-reacting case. These quantities should consider additional coupled contributions related to specific response variables defined for reacting cases such as combustion efficiency and/or even emissions levels.

Declaration of competing interest

The authors declare that they have no known competing financial interests or personal relationships that could have appeared to influence the work reported in this paper.

Acknowledgements

Appendix A. Full set of results for the L9 orthogonal array parametric study on the geometrical features

See Figs. A.13–A.17 for the full set of results of the parametric study provided by the L9 orthogonal array.

References

[1] R.M.A. Valdés, S. Burmaoglu, V. Tucci, L.M.B. da Costa Campos, L. Mattera, V.F.G. Comendador, Flight path 2050 and ACARE goals for maintaining and extending industrial leadership in aviation: a map of the aviation technology space, Sustainability 11 (2019) 2065, https://doi.org/10.3390/su11072065.

[2] X. Liu, A.M. Elbaz, C. Gong, X.S. Bai, H.T. Zheng, W.L. Roberts, Effect of burner geometry on swirl stabilized methane/air flames: a joint les/oh-plif/piv study, Fuel 207 (2017) 533–546, https://doi.org/10.1016/j.fuel.2017.06.092.

[3] G.E. Ballachey, M.R. Johnson, Prediction of blowoff in a fully controllable low-swirl burner burning alternative fuels: effects of burner geometry, swirl, and fuel composition, Proc. Combust. Inst. 34 (2013) 3193–3201, https://doi.org/10.1016/j.proci.2012.05.095.

[4] M. Saediamiri, M. Birouk, J.A. Kozinski, Flame stability limits of low swirl burner: effect of fuel composition and burner geometry, Fuel 208 (2017) 410–422, https://doi.org/10.1016/j.fuel.2017.07.028.

[5] R. Yuan, J. Kariuki, E. Mastorakos, Measurements in swirling spray flames at blow-off, Int. J. Spray Combust. Dyn. 10 (2018) 185–210, https://doi.org/10.1177/1756827718763559.

[6] D. Barré, M. Kraushaar, G. Staffelbach, V. Moureau, L.Y. Gicquel, Compressible and low Mach number LES of a swirl experimental burner, C. R. Mecanique 341 (2013) 277–287, https://doi.org/10.1016/j.crme.2012.11.010.

[7] F. Collin-Bastiani, J. Marrero-Santiago, E. Riber, G. Cabot, B. Renou, B. Cuenot, A joint experimental and numerical study of ignition in a spray burner, Proc. Combust. Inst. 37 (2019) 5047–5055, https://doi.org/10.1016/j.proci.2018.05.132.

[8] J. Marrero-Santiago, F. Collin-Bastiani, E. Riber, G. Cabot, B. Cuenot, B. Renou, On the mechanisms of flame kernel extinction or survival during aeronautical ignition sequences: experimental and numerical analysis, Combust. Flame 222 (2020) 70–84, https://doi.org/10.1016/j.combustflame.2020.08.021.

[9] S. Joo, S. Kwak, J. Lee, Y. Yoon, Thermoacoustic instability and flame transfer function in a lean direct injection model gas turbine combustor, Aerosp. Sci. Technol. 116 (2021) 106872, https://doi.org/10.1016/j.ast.2021.106872.

[10] J. Cai, S.-M. Jeng, R. Tacina, The structure of a swirl-stabilized reacting spray issued from an axial swirler, in: 43rd AIAA Aerospace Sciences Meeting and Exhibit, American Institute of Aeronautics and Astronautics, 2005.

[11] J.D. Gounder, A. Kourmatzis, A.R. Masri, Turbulent piloted dilute spray flames: flow fields and droplet dynamics, Combust. Flame 159 (2012) 3372–3397, https://doi.org/10.1016/j.combustflame.2012.07.014.

[12] R. Hadef, B. Lenze, Measurements of droplets characteristics in a swirl-stabilized spray flame, Exp. Therm. Fluid Sci. 30 (2005) 117–130, https://doi.org/10.1016/j.expthermflusci.2005.05.002.

[13] A.R. Masri, J.D. Gounder, Turbulent spray flames of acetone and ethanol approaching extinction, Combust. Sci. Technol. 182 (2010) 702–715, https://doi.org/10.1080/00102200903467754.
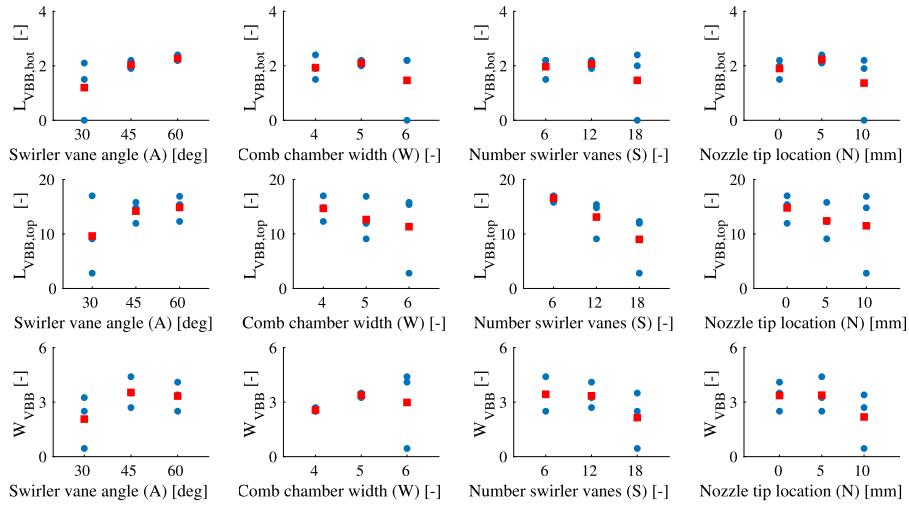
Fig. A.13. Dispersion values of the response variables for each design parameter (1 of 5). Blue circles: the values of the response variable for each of the 9 simulations. Red squares: average of the 3 values for each level of the considered geometric factor.
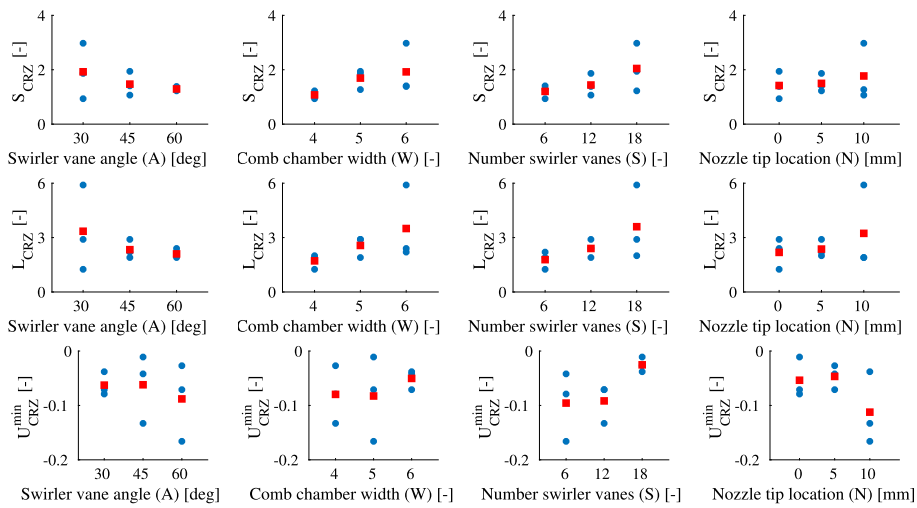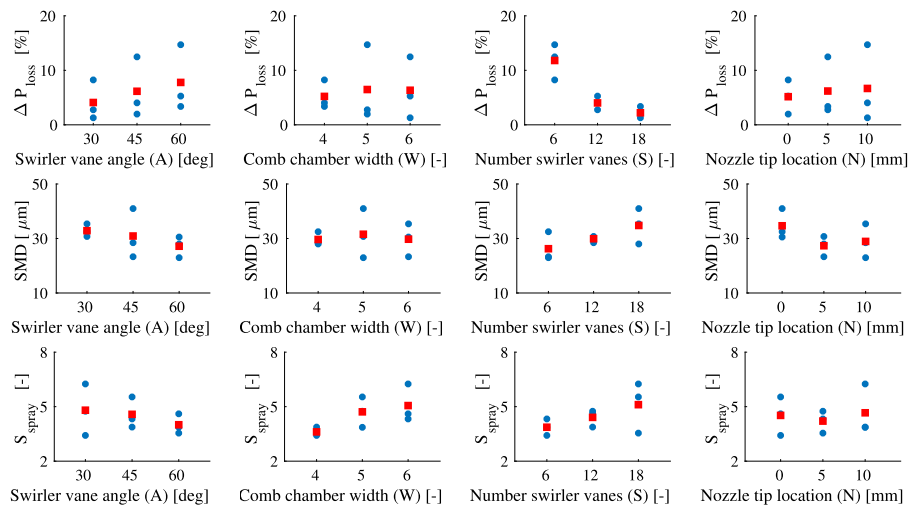

Fig. A.14. Dispersion values of the response variables for each design parameter (2 of 5). Blue circles: the values of the response variable for each of the 9 simulations. Red squares: average of the 3 values for each level of the considered geometric factor.
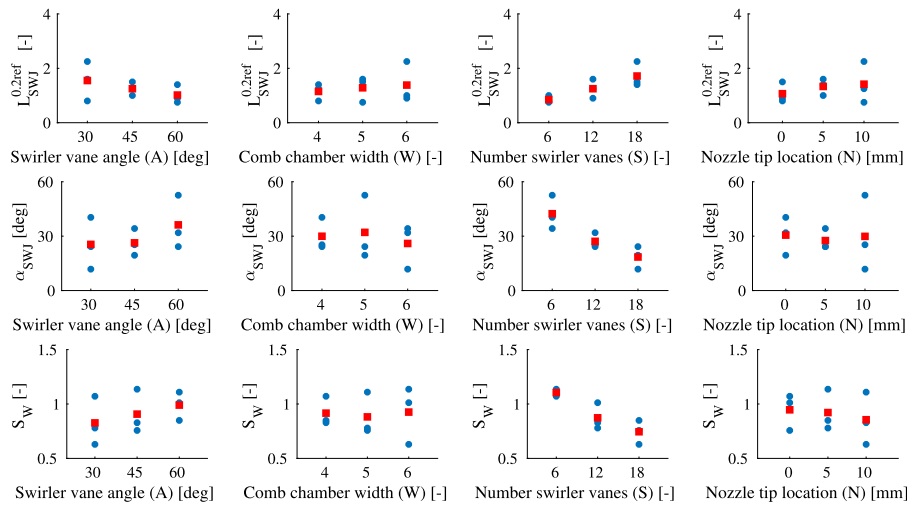

Fig. A.15. Dispersion values of the response variables for each design parameter (3 of 5). Blue circles: the values of the response variable for each of the 9 simulations. Red squares: average of the 3 values for each level of the considered geometric factor.

Fig. A.16. Dispersion values of the response variables for each design parameter (4 of 5). Blue circles: the values of the response variable for each of the 9 simulations. Red squares: average of the 3 values for each level of the considered geometric factor.
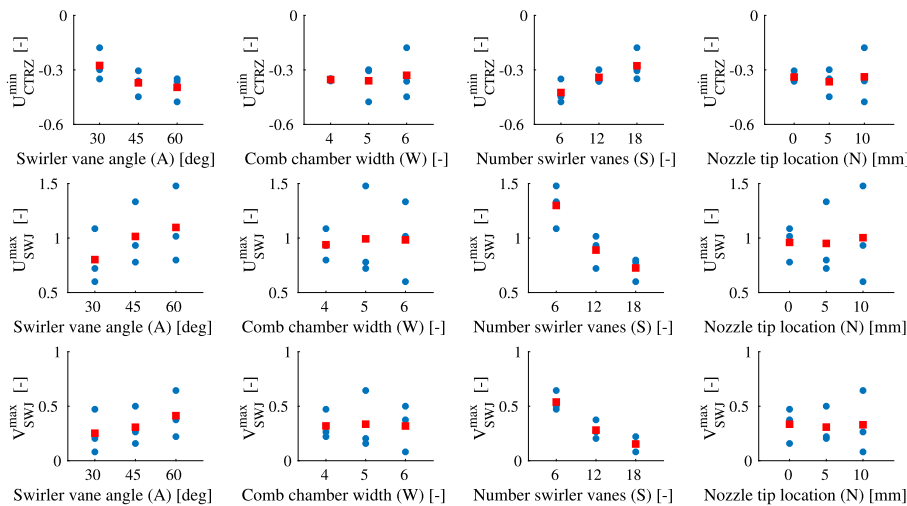

Fig. A.17. Dispersion values of the response variables for each design parameter (5 of 5). Blue circles: the values of the response variable for each of the 9 simulations. Red squares: average of the 3 values for each level of the considered geometric factor.

[14] I.A. Mulla, G. Godard, G. Cabot, F. Grisch, B. Renou, Quantitative imaging of nitric oxide concentration in a turbulent n-heptane spray flame, Combust. Flame 203 (2019) 217–229, https://doi.org/10.1016/j.combustflame.2019.02.005.

[15] I.A. Mulla, B. Renou, Simultaneous imaging of soot volume fraction, pah, and oh in a turbulent n-heptane spray flame, Combust. Flame 209 (2019) 452–466, https://doi.org/10.1016/j.combustflame.2019.08.012.

[16] I.A. Mulla, G. Godard, B. Renou, Instantaneous planar measurements of nitric oxide concentration in a turbulent n-heptane spray flame, Combust. Flame 208 (2019) 451–471, https://doi.org/10.1016/j.combustflame.2019.07.026.

[17] M. Legrand, J. Nogueira, A. Lecuona, S. Nauri, P.A. Rodríguez, Atmospheric low swirl burner flow characterization with stereo PIV, Exp. Fluids 48 (2010) 901–913, https://doi.org/10.1007/s00348-009-0775-6.

[18] Y. Huang, V. Yang, Dynamics and stability of lean-premixed swirl-stabilized combustion, Prog. Energy Combust. Sci. 35 (2009) 293–364, https://doi.org/10.1016/j.pecs.2009.01.002.

[19] M. Sanjosé, J.M. Senoner, F. Jaegle, B. Cuenot, S. Moreau, T. Poinsot, Fuel injection model for Euler-Euler and Euler-Lagrange large-eddy simulations of an evaporating spray inside an aeronautical combustor, Int. J. Multiph. Flow 37 (2011) 514–529, https://doi.org/10.1016/j.ijmultiphaseflow.2011.01.008.

[20] F. Jaegle, J.M. Senoner, M. García, F. Bismes, R. Lecourt, B. Cuenot, T. Poinsot, Eulerian and Lagrangian spray simulations of an aeronautical multipoint injector, Proc. Combust. Inst. 33 (2011) 2099–2107, https://doi.org/10.1016/j.proci.2010.07.027.

[21] W.P. Jones, C. Lettieri, A.J. Marquis, S. Navarro-Martinez, Large eddy simulation of the two-phase flow in an experimental swirl-stabilized burner, Int. J. Heat Fluid Flow 38 (2012) 145–158, https://doi.org/10.1016/j.ijheatfluidflow.2012.09.001.

[22] M. Boileau, S. Pascaud, E. Riber, B. Cuenot, L.Y.M. Gicquel, T.J. Poinsot, M. Cazalens, Investigation of two-fluid methods for large eddy simulation of spray combustion in gas turbines, Flow Turbul. Combust. 80 (2008) 291–321, https://doi.org/10.1007/s10494-007-9123-1.

[23] A. Panchal, S. Menon, Large eddy simulation of fuel sensitivity in a realistic spray combustor I. Near blowout analysis, Combust. Flame (2022) 112162, https://doi.org/10.1016/j.combustflame.2022.112162.

[24] W.P. Jones, A.J. Marquis, K. Vogiatzaki, Large-eddy simulation of spray combustion in a gas turbine combustor, Combust. Flame 161 (2014) 222–239, https://doi.org/10.1016/j.combustflame.2013.07.016.

[25] P. Wang, S.M. Hashemi, H. He, K. Cheng, Investigation of the partially premixed turbulent combustion through the PRECCINSTA burner by large eddy simulation, Aerosp. Sci. Technol. 121 (2022) 107336, https://doi.org/10.1016/j.ast.2022.107336.

[26] S. Puggelli, D. Bertini, L. Mazzei, A. Andreini, Modeling strategies for large eddy simulation of lean burn spray flames, J. Eng. Gas Turbines Power 140 (5) (2018) 051501, https://doi.org/10.1115/1.4038127.

[27] D. Mira, O. Lehmkuhl, A. Both, P. Stathopoulos, T. Tanneberger, T.G. Reichel, C.O. Paschereit, M. Vázquez, G. Houzeaux, Numerical characterization of a premixed hydrogen flame under conditions close to flashback, Flow Turbul. Combust. 104 (2–3) (2020) 479–507, https://doi.org/10.1007/s10494-019-00106-z.

[28] L. Palanti, A. Andreini, B. Facchini, Numerical prediction of the ignition probability of a lean spray burner, Int. J. Spray Combust. Dyn. 13 (1–2) (2021) 96–109, https://doi.org/10.1177/17568277211012536.

[29] D.G. Lilley, Swirl flows in combustion: a review, AIAA J. 15 (1977) 1063–1078, https://doi.org/10.2514/3.60756.

[30] N.A. Chigier, J.M. Beer, Velocity and static-pressure distributions in swirling

air jets issuing from annular and divergent nozzles, J. Basic Eng. 86 (1964) 788–796, https://doi.org/10.1115/1.3655954.

[31] K.S. Im, H. Kim, M.C. Lai, R. Tacina, Parametric study of the swirler/venturi spray injectors, J. Propuls. Power 17 (2001) 717–727, https://doi.org/10.2514/2.5801.

[32] C.M. Heath, Characterization of swirl-venturi lean direct injection designs for aviation gas turbine combustion, J. Propuls. Power 30 (2014) 1334–1356, https://doi.org/10.2514/1.B35077.

[33] K.M. Tacina, P. Lee, H. Mongia, B.K. Dam, Z.J. He, D.P. Podboy, A comparison of three second-generation swirl-venturi lean direct injection combustor concepts, in: 52nd AIAA/SAE/ASEE Joint Propulsion Conference, American Institute of Aeronautics and Astronautics, 2016.

[34] A.K. Gupta, M.S. Ramavajjala, J. Chomiak, N. Marchionna, Burner geometry effects on combustion and NOx emission characteristics using a variable geometry swirl combustor, J. Propuls. Power 7 (1991) 473–480, https://doi.org/10.2514/3.23351.

[35] C.W. Lee, S.Y. Moon, An experimental investigation of the effects of turbulence generators attached to an axial swirler nozzle on mixing and combustion, Aerosp. Sci. Technol. 6 (2002) 517–520, https://doi.org/10.1016/S1270-9638(02)01164-1.

[36] S.A. Tedder, K.M. Tacina, R.C. Anderson, Y.R. Hicks, Fundamental study of a single point lean direct injector. Part I: effect of air swirler angle and injector tip location on spray characteristics, in: 50th AIAA/ASME/SAE/ASEE Joint Propulsion Conference, 2014, pp. 2014–3435.

[37] S. Sharma, K. Ghate, T. Sundararajan, S. Sahu, Effects of air swirler geometry on air and spray droplet interactions in a spray chamber, Adv. Mech. Eng. 11 (2019) 1–15, https://doi.org/10.1177/1687814019850978.

[38] X. Ren, X. Xue, K.B. Brady, C.J. Sung, H.C. Mongia, The impact of swirling flow strength on lean-dome LDI pilot mixers' operability and emissions, Exp. Therm. Fluid Sci. 109 (2019) 109840, https://doi.org/10.1016/j.expthermflusci.2019.109840.

[39] X. Ren, K.B. Brady, X. Xue, C.J. Sung, H.C. Mongia, Experimental investigation of lean-dome high-airflow airblast pilot mixers' operability, emissions, and dynamics, Aerosp. Sci. Technol. 100 (2020) 105829, https://doi.org/10.1016/j.ast.2020.105829.

[40] K. Oberleithner, C.O. Paschereit, R. Seele, I. Wygnanski, Formation of turbulent vortex breakdown: intermittency, criticality, and global instability, AIAA J. 50 (2012) 1437–1452, https://doi.org/10.2514/1.J050642.

[41] Y. Wu, C. Carlsson, R. Szasz, L. Peng, L. Fuchs, X.S. Bai, Effect of geometrical contraction on vortex breakdown of swirling turbulent flow in a model combustor, Fuel 170 (2016) 210–225, https://doi.org/10.1016/j.fuel.2015.12.035.

[42] F.F. Grinstein, C. Fureby, LES studies of the flow in a swirl gas combustor, Proc. Combust. Inst. 30 (II) (2005) 1791–1798, https://doi.org/10.1016/j.proci.2004.08.082.

[43] C.E. Lee, S.H. Park, C.H. Hwang, Numerical study of the effect of inlet geometry on combustion instabilities in a lean premixed swirl combustor, J. Mech. Sci. Technol. 30 (2016) 5293–5303, https://doi.org/10.1007/s12206-016-1048-y.

[44] K. Mazaheri, A. Shakeri, Numerical optimization of laboratory combustor geometry for NO suppression, Appl. Therm. Eng. 102 (2016) 1328–1336, https://doi.org/10.1016/j.applthermaleng.2016.04.027.

[45] R.M. Gejji, C. Huang, C. Fugger, C. Yoon, W. Anderson, Parametric investigation of combustion instabilities in a single-element lean direct injection combustor, Int. J. Spray Combust. Dyn. 11 (2018) 1–16, https://doi.org/10.1177/1756827718785851.

[46] F.A. Williams, Combustion Theory, CRC Press, 1985.

[47] A. Broatch, M. Carreres, J. García-Tíscar, M. Belmar-Gil, Spectral analysis and modelling of the spray liquid injection in a Lean Direct Injection (LDI) gas turbine combustor through Eulerian-Lagrangian Large Eddy Simulations, Aerosp. Sci. Technol. 118 (2021) 106992, https://doi.org/10.1016/j.ast.2021.106992.

[48] R. Payri, R. Novella, M. Carreres, M. Belmar-Gil, Modeling gaseous non-reactive flow in a lean direct injection gas turbine combustor through an advanced mesh control strategy, Proc. Inst. Mech. Eng., Part G, J. Aerosp. Eng. 234 (2020) 1788–1810, https://doi.org/10.1177/0954410020919619.

[49] J. Smagorinsky, General circulation experiments with the primitive equations, Mon. Weather Rev. 91 (3) (1963) 99–164, https://doi.org/10.1175/1520-0493(1963)091<0099:GCEWTP>2.3.CO;2.

[50] M. Germano, U. Piomelli, P. Moin, W.H. Cabot, A dynamic subgrid-scale eddy viscosity model, Phys. Fluids A 3 (1991) 1760–1765, https://doi.org/10.1063/1.857955.

[51] P.J. O'Rourke, A.A. Amsden, The tab method for numerical calculation of spray droplet breakup, in: SAE International Fall Fuels and Lubricants Meeting and Exhibition, 1987.

[52] A.B. Liu, D. Mather, R.D. Reitz, Modeling the effects of drop drag and breakup on fuel sprays, in: SAE International Congress and Exposition, vol. 298, 1993, pp. 1–6.

[53] C. Crowe, J. Chung, T. Troutt, Particle mixing in free shear flows, Prog. Energy Combust. Sci. 14 (1988) 171–194, https://doi.org/10.1016/0360-1285(88)90008-1.

[54] P.J. O'Rourke, Collective drop effects on vaporizing liquid sprays, Ph.D. thesis, Princeton University, 1981.

[55] A.A. Amsden, P.J. O'Rourke, T.D. Butler, Kiva-ii: a computer program for chemically reactive flows with sprays, Report, Los Alamos National Laboratory (LANL), 1989, http://www.osti.gov/servlets/purl/6228444/, 2021.

[56] J. Marrero-Santiago, Experimental study of lean aeronautical ignition. Impact of critical parameters on the mechanisms acting along the different ignition phases, Ph.D. thesis, INSA de Rouen - Normandie, 2018.

[57] J. Marrero-Santiago, A. Verdier, C. Brunet, A. Vandel, G. Godard, G. Cabot, M. Boukhalfa, B. Renou, Experimental study of aeronautical ignition in a swirled confined jet-spray burner, J. Eng. Gas Turbines Power 140 (2) (2018) 021502, https://doi.org/10.1115/1.4037752.

[58] J. Marrero-Santiago, A. Verdier, G. Godard, A. Vandel, G. Cabot, A.M. Boukhalfa, B. Renou, Experimental study of airflow velocity, fuel droplet size-velocity and flame structure in a confined swirled jet-spray flame, in: ILASS - Europe 2016, Brighton, England, 2016.

[59] F. Collin-Bastiani, J. Marrero-Santiago, A. Verdier, A. Vandel, G. Cabot, E. Riber, S. Richard, A. Cayre, B. Renou, B. Cuenot, On the extinction and ignition mechanisms along the ignition events in the kiai spray burner. A joint experimental and numerical approach, in: 4e Colloque du reseau d'INitiative en Combustion Avancee (INCA), Paliseau, France, 2017.

[60] D.A. Alessandro, I. Stankovic, B. Merci, LES study of a turbulent spray jet: mesh sensitivity, mesh-parcels interaction and injection methodology, Flow Turbul. Combust. 103 (2019) 537–564, https://doi.org/10.1007/s10494-019-00039-7.

[61] H. Wengle, H. Werner, Large-eddy simulation of turbulent flow over sharp-edged obstacles in a plate channel, in: K. Gersten (Ed.), Physics of Separated Flows - Numerical, Experimental, and Theoretical Aspects, in: Notes on Numerical Fluid Mechanics (NNFM), vol. 40, 1993.

[62] C.M. Rhie, W.L. Chow, Numerical study of the turbulent flow past an airfoil with trailing edge separation, AIAA J. 21 (1983) 1525–1532, https://doi.org/10.2514/3.8284.

[63] H. Abdi, L.J. Williams, Principal component analysis, Wiley Interdiscip. Rev.: Comput. Stat. 2 (4) (2010) 433–459, https://doi.org/10.1002/wics.101.

[64] F.J. Salvador, M. Carreres, J. García-Tíscar, M. Belmar-Gil, Modal decomposition of the unsteady non-reactive flow field in a swirl-stabilized combustor operated by a lean premixed injection system, Aerosp. Sci. Technol. 112 (2021) 106622, https://doi.org/10.1016/j.ast.2021.106622.

[65] H. Nyquist, Regeneration theory, Bell Syst. Tech. J. (1932) 11, https://doi.org/10.1002/j.1538-7305.1932.tb02344.x.

[66] J.L. Bentley, Multidimensional binary search trees used for associative searching, Commun. ACM 18 (1975) 509–517, https://doi.org/10.1145/361002.361007.

[67] J.H. Friedman, J.L. Bentley, R.A. Finkel, An algorithm for finding best matches in logarithmic expected time, ACM Trans. Math. Softw. 3 (1977) 209–226, https://doi.org/10.1145/355744.355745.

[68] P.J. Ross, Taguchi Techniques for Quality Engineering: Loss Function, Orthogonal Experiments, Parameter and Tolerance Design, McGraw Hill, New York, 1998.

[69] F.J. Salvador, M. Carreres, M. Crialesi-Esposito, A.H. Plazas, Determination of critical operating and geometrical parameters in diesel injectors through one dimensional modelling, design of experiments and an analysis of variance, Proc. Inst. Mech. Eng., Part D, J. Automob. Eng. 232 (2018) 1762–1781, https://doi.org/10.1177/0954407017735262.

[70] A.H. Lefebvre, D.R. Ballal, Gas Turbine Combustion: Alternative Fuels and Emissions, CRC Press, 2010.

[71] A. Valera-Medina, N. Syred, P. Kay, A. Griffiths, Central recirculation zone analysis in an unconfined tangential swirl burner with varying degrees of premixing, Exp. Fluids 50 (2011) 1611–1623, https://doi.org/10.1007/s00348-010-1017-7.